Thesis

ASSESSMENT OF BRAIN VISCOELASTICITY IN MULTIPLE SCLEROSIS USING MAGNETIC RESONANCE ELASTOGRAPHY –
AN EXPLORATORY STUDY

submitted by
Christian KISS

in partial Fulfillment of the Requirements for the Degree of
Doctor of Medicine
(Dr. med. univ.)

at the
Medical University of Graz

executed on the
Department of Neurology
Division of General Neurology

under the Supervision of
Assoz. Prof. Univ.-Doz. Dipl.-Ing. Dr. Stefan ROPELE

Graz, 11 November 2021

Statutory Declaration

I hereby declare that this thesis is my own original work and that I have fully acknowledged by name all of those individuals and organisations that have contributed to the research for this thesis. Due acknowledgement has been made in the text to all other material used. Throughout this thesis and in all related publications I followed the "Guidelines of the Medical University of Graz on Good Scientific Practice".

Graz, 11 November 2021 Christian Kiss m.p.

Acknowledgments

I would like to take this opportunity to thank all the individuals who supported me in the process of writing this thesis.

First and foremost, I want to express my sincere gratitude to my supervisor, Prof. Stefan Ropele. He provided me excellent guidance and feedback in each step throughout this challenging project. I am very thankful for all the insightful discussions, which truly aroused my curiosity in neuroimaging and motivate me to do further research in this area.

I am deeply indebted to Dr. Johannes Strasser who tirelessly helped me in grasping the fascinating concepts behind MRI and elastography. He always supported me in my imaging analyses and far beyond.

I would like to extend my sincere thanks to Prof. Daniela Pinter for her advice on statistics and good scientific practice. Her expertise and helpfulness are truly remarkable.

I am grateful to my whole family for their constant support during my medical studies. I wholeheartedly thank my sister Joanna, who is the linguistic genius in our family, for her constructive suggestions. Thank you for your help and our little journey through the quirks of the English language!

Finally and most importantly, I want to thank my girlfriend Elena. You always had an open ear for my thoughts and helped me to maintain my sanity. Your love and emotional support has meant more to me than words could possibly say.

Table of Contents

List of Abbreviations

AFM	Atomic Force Microscopy
BBB	Blood-Brain Barrier
CIS	Clinically Isolated Syndrome
CNS	Central Nervous System
CSF	Cerebrospinal Fluid
DWI	Diffusion Weighted Imaging
ECM	Extracellular Matrix
EDSS	Expanded Disability Status Scale
EPI	Echo Planar Imaging
FLAIR	Fluid Attenuated Inversion Recovery
fMRI	Functional Magnetic Resonance Imaging
FSL	FMRIB Software Library
GM	Grey Matter
HC	Healthy Control
Hz	Hertz
IQR	Interquartile Range
LPA	Lesion Progression Algorithm
LST	Lesion Segmentation Toolbox
LVER	Linear Viscoelastic Region
MDEV	Multifrequency Dual Elasto-Visco Inversion
MRE	Magnetic Resonance Elastography
MRI	Magnetic Resonance Imaging
MS	Multiple Sclerosis
MSFC	Multiple Sclerosis Functional Composite
NAWM	Normal-Appearing White Matter
NBV	Normalized Brain Volume
NEDA	No Evidence of Disease Activity
NV$_{ROI}$	Normalized Volume in Region of Interest
Pa	Pascal
PPMS	Primary Progressive Multiple Sclerosis
rad	Radian
ROI	Region of Interest
RRMS	Relapsing-Remitting Multiple Sclerosis
SD	Standard Deviation
SGM	Subcortical Grey Matter

SPMS	Secondary Progressive Multiple Sclerosis
SWI	Susceptibility Weighted Imaging
T1w	T1-Weighted Imaging
T2w	T2-Weighted Imaging
TE	Time to Echo
TI	Time to Inversion
TM	Mixing Time
TR	Time to Repetition
WM	White Matter
WMH	White Matter Hyperintensities

List of Symbols

G^*	Complex shear modulus
$\lvert G^*\rvert$	Magnitude of the complex shear modulus
G'	Storage modulus, or real part of the complex shear modulus
G''	Loss modulus, or imaginary part of the complex shear modulus
α	Interpolation factor in a springpot model
μ	Shear stiffness in a springpot model
ξ	Damping ratio
φ	Phase angle of the complex shear modulus

List of Figures

List of Tables

Zusammenfassung

Einleitung Die Magnetresonanzelastographie (MRE) ist ein nicht-invasives Bildgebungsverfahren, welches das Verhalten von Gewebe bei mechanischer Anregung misst. Dadurch lässt sich die Viskoelastizität von Gewebe bestimmen, die durch pathologische Prozesse verändert sein kann. Bei Multipler Sklerose (MS) gehen akut inflammatorische mit chronisch neurodegenerativen Prozessen einher. Durch konventionelle Magnetresonanztomographie (MRT) können diese Vorgänge nur unzureichend dargestellt werden. Das klinische Bild entspricht zudem häufig nicht dem radiologischen Korrelat. Messungen verschiedener Gewebe haben bereits gezeigt, dass MRE sensitiv für feine strukturelle Veränderungen ist. MRE ist deshalb eine vielversprechende Modalität, um den Krankheitsverlauf bei MS besser vorherzusagen und zu quantifizieren. Ziel dieser Studie war es zu untersuchen, ob MRE mikrostrukturelle Veränderungen bei MS *in vivo* darstellen kann, und zu bewerten, ob MRE zur paraklinischen Untersuchung von MS-PatientInnen und zum Verständnis der pathologischen Vorgänge bei MS beitragen kann.

Methoden In einer kontrollierten Studie wurden 73 MS-PatientInnen und 42 gesunde Freiwillige magnetresonanztomographisch untersucht. Die Elastographie erfolgte im Großhirn mittels einer bewegungssensitiven stimulierten-Echo-Sequenz (DENSE) bei einer mechanischen Anregung von 20 Hertz. Magnitude $|G^*|$ und Phasenwinkel φ des komplexen Schermoduls G^* wurden mit multi-frequency dual-elastico inversion (MDEV) rekonstruiert. T1- und T2-gewichtete strukturelle Sequenzen dienten der anatomischen Orientierung und MS-Läsionsanalyse. Gemittelte Messwerte verschiedener Gehirnareale wurden zwischen beiden Kohorten verglichen und in Bezug zu demographischen, klinischen und radiologischen Parametern gesetzt.

Ergebnisse Eine multiple Regressionsanalyse zeigte, dass bei MS in der subkortikalen grauen Substanz Alter und Atrophie mit einer Verkleinerung von φ korrelieren ($p < 0.001$). Die Erkrankungsdauer war mit einer Reduktion von $|G^*|$ assoziiert ($p = 0.01$). Der Behinderungsgrad (EDSS) zeigte keinen Zusammenhang zur Viskoelastizität unter Berücksichtigung des Alters. Die Viskoelastizität von Läsionen war relativ zur normal erscheinenden weißen Substanz im Wesentlichen unverändert, gleichsam korrelierten Läsionslast und Hirnelastizität nicht. Zwischen beiden Kohorten war kein Unterschied der Viskoelastizität auf Gewebeebene feststellbar, allerdings zeigte sich eine signifikante Verkleinerung von φ im Thalamus bei MS ($p = 0.002$).

Fazit MRE kann mikrostrukturelle Veränderungen von Hirngewebe bei MS nachweisen, zeigt für den klinischen Einsatz derzeit aber keine ausreichende Sensitivität und Spezifität.

Abstract

Introduction Magnetic resonance elastography (MRE) is an imaging modality that non-invasively gauges the response of tissue to mechanical excitation. Thereby, it objectively quantifies the viscoelasticity of tissue, which can be altered by pathological processes. In multiple sclerosis (MS), acute inflammation is accompanied by chronic neurodegeneration. However, radiological findings in conventional magnetic resonance imaging (MRI) only poorly reflect these processes and lack correlation with clinical presentation. MRE has already proven sensitivity to subtle alterations in various types of tissue, making it a promising modality to better predict and monitor progression of MS. The purpose of this study was to explore whether MRE can reveal viscoelasticity changes in the *in vivo* MS brain. It was further evaluated if MRE can contribute to paraclinical assessment of MS patients and to understanding of pathological processes in MS.

Methods In a controlled study, 73 MS patients and 42 healthy volunteers underwent MRI examination. Cerebral MRE was performed using a motion-sensitive stimulated echo sequence (DENSE) with a mechanical excitation at 20 Hertz. Magnitude $|G^*|$ and phase angle φ of the complex shear modulus G^* were reconstructed by multi-frequency dual-elastico inversion (MDEV). T1- and T2-weighted structural images were acquired for tissue segmentation, brain atrophy estimation and MS lesion analysis. Region of interest-based means in viscoelasticity were compared between cohorts and related to demographic, clinical and radiological characteristics.

Results In the subcortical grey matter of MS patients, according to a multiple regression analysis, age and atrophy correlated with a decrease in φ ($p < 0.001$). Disease duration was associated with a reduction in $|G^*|$ in white matter ($p = 0.01$). Disability was not related to viscoelasticity after accounting for age. There was neither a relevant alteration in viscoelasticity in lesions relative to the normal appearing white matter, nor was lesion load associated with brain viscoelasticity. Between cohorts, no difference in brain viscoelasticity was found on tissue level. However, a significant decrease in φ in the thalamus was observed in MS ($p = 0.002$).

Conclusion MRE can reveal microstructural alterations in the MS brain but lacks sensitivity and specificity to complement clinical assessment to date.

1 Introduction

Many diseases impact the structural integrity of biological tissue by various pathological processes, among others neoplasia, inflammation or fibrosis. Changes in tissue structure can frequently be identified through manual palpation at early stages, which is why palpation is one of the oldest examination techniques and a valuable tool in the clinical assessment to date [1].

In the process of palpation, layers of tissue are displaced against each other, leading to a tensed state of structural elements. This tension resists further deformation by the physician's hand, which can be perceived as stiffness. However, palpation is only a semi-quantitative measurement of stiffness and is highly subjective to the physician. Furthermore, many organs are not accessible to the physician's hand, most notably the brain.

1.1 Multiple Sclerosis

Multiple sclerosis (MS) is a chronic inflammatory and neurodegenerative disease of the central nervous system (CNS). One hallmark of MS is demyelination, in which myelin sheaths of axons are attacked by the immune system. Today, MS affects approximately 2.5 million people globally. With an incidence peaking between 20 and 40 years, MS is the leading cause of nontraumatic disability among young adults in Europe and North America [2].

The underlying pathological processes of MS are complex, vary over time and differ among patients, giving rise to different courses of disease [3]. The clinically isolated syndrome (CIS) designates the first occurence of neurological deficits suggestive of MS due to focal demyelination. Identification of predictive factors for conversion from CIS to clinically definitive MS is of high relevance for early treatment and matter of active research [4, 5]. Relapsing-remitting MS (RRMS) is the most common disease course, in which patients present with a pattern of relapses and remissions. A relapse is defined as a flare of neurological symptoms limited to a period of time and is typically accompanied by characteristic radiological correlates. The progressive phenotype comprises primary progressive MS (PPMS) and secondary progressive MS (SPMS), in which persistent clinical worsening independent of relapse activity is present [6].

Whereas focal demyelination predominates relapsing disease courses, diffuse neurodegeneration plays a major role in progressive MS phenotypes [6]. Neurodegeneration involves neuronal and axonal loss and is considered as the major driving mechanism to long-term disability, which is why it gained increasing attention in research. However, the pathological processes promoting diffuse neurodegeneration are not fully understood to date. Moreover, there is growing evidence from neuroimaging and pathology that even in relapsing phenotypes, diffuse injury is present at early stages of disease [7, 8].

Albeit no cure is in sight, effective disease-modifying treatments (DMTs) have been developed, which significantly reduce relapse rate and delay progression of disease [9, 10]. In order to find the best therapy for an individual patient, reliable tools for early diagnosis, prediction of disease progression and evaluation of treatment efficacy are needed. That is why next to clinical examination [11], complementary paraclinical tools have been adopted, most notably magnetic resonance imaging (MRI) [12]. As reflected in MS diagnostic criteria, MRI plays a key role in MS diagnosis and has its fix place in routine follow-up assessment [6, 12, 13].

1.2 Neuroimaging in Multiple Sclerosis

The use of MRI in MS presupposes a close association between radiological abnormalities and disease in order to derive meaningful information. However, MRI has limited diagnostic specificity [14, 15] and only poorly correlates with disability, coining the term ‘clinico-radiologic paradox’ [16–19]. In fact, MRI is highly sensitive to focal inflammatory processes, which acutely present as contrast-enhancing lesions in T1-weighted (T1w) images and persist as chronic lesions in T2-weighted (T2w) images. However, microstructural parenchymal damage, which procures diffuse neurodegeneration, is generally hidden in an MRI scan. That is why in neuroimaging, white matter (WM) in the absence of lesions is referred to as normal-appearing white matter (NAWM) [20].

In order to improve assessment and prognosis of disease, much effort has been put in the development of various advanced MRI techniques, which aim at reflecting micro- and macrostructural as well as metabolic features of MS [17]. Although advanced modalities are still lacking routine clinical use, they considerably contribute to understanding of disease, unravel the complex interaction of pathological processes *in vivo* and play an important role in evaluation of efficacy in DMT studies.

For instance, MRI spectroscopy considerably accounted for a paradigm shift in research from inflammatory demyelination to neurodegenerative processes by quantifying axonal damage and its role for disability [21, 22]. Brain volumetry assesses brain atrophy as a surrogate for global parenchymal damage, since atrophy has proven to correlate well with disability and to predict future clinical worsening [23–25]. Sensitive to axonal damage, diffusion tensor imaging (DTI) contributes to NAWM damage assessment and has suggested that diffuse neurodegeneration is even present in RRMS patients who show no evidence of disease activity (NEDA) [26].

1.3 Elastography

In medical imaging, quantitative equivalents to palpation have been developed, referred to as elastography. Elastography non-invasively derives the mechanical properties of tissue by measuring the tissue's deformation under mechanical stress. To date, two technologies have emerged: ultrasound elastography and magnetic resonance elastography (MRE) [27, 28]. Elastography not only differentiates between stiff and soft, but also gauges a material's viscous and elastic properties, summarized as viscoelasticity [29, 30].

It is well known from material science and *ex vivo* rheological experiments that the viscoelasticity of biological tissue is defined by its microstructural properties [30, 31]. As exploited by palpation, a change in stiffness indicates an underlying change in microstructure, which potentially relates to a pathological process. This suggests elastography as a promising tool for non-invasive diagnosis and assessment of diseases.

In the human body, stiffness parameters range from 0 Pascal (Pa) in liquids to more than 10 GPa in bone, which equals a 10-fold increase in orders of magnitude [32]. This number reflects the broad variety of mechanical properties in different kinds of tissue with a contrast range surpassing that of other imaging modalities, such as MRI relaxation times [33] or Hounsfield units in computer tomography [34]. Similarly, stiffness can vary significantly when tissue undergoes a pathological process. E.g., a healthy mammary gland exhibits a stiffness of approximately 150 Pa, whereas in mammary tumors, measures range around 4000 Pa [35].

1.4 Magnetic Resonance Elastography

Since its first description in 1995 by Muthupillai et al. [36], MRE has demonstrated high sensitivity to pathological changes in various organs [27, 37–42]. Today, MRE is already well-established in the assessment of liver fibrosis and considered as the most accurate non-invasive method for diagnosis and quantification of chronic liver disease [27, 43, 44].

First MRE experiments of the *in vivo* human brain have been published in 2007 and 2008 [28, 44–46]. Meanwhile, MRE in brain has continuously evolved and is subject of active research, as indiciated by an increasing number of publications [47, 48]. Although the use of MRE with regard to the brain is still in its infancy, MRE has already delivered promising results in the investigation of a range of neurological diseases.

For instance, MRE has been used to assess stiffness alterations in normal pressure hydrocephalus [49] and to help differentiating between entities of intracranial tumors [50]. In neuroinflammatory and neurodegenerative disorders such as MS, Alzheimer's disease and dementia, using MRE, pathological alterations in viscoelasticity of brain tissue have been revealed [51–56].

To date, only few MRE studies investigating the MS brain exist. Studies conducted by Wuerfel et al. [54] and Streitberger et al. [51] suggested a significant decrease in global brain stiffness in MS patients compared to a matched healthy control (HC) group. Although less pronounced, this was also shown for CIS patients [57]. These findings are supported by *ex vivo* experiments, which revealed two stiffness altering mechanisms applicable to processes found in MS. In a study on bovine brains, it was suggested that brain stiffness is proportionally correlated to myelin content [58]. Another study revealed that glial scar tissue is significantly lower in stiffness than healthy brain tissue [59], which was attributed to a lack in supporting collagen-1 in the upregulated extracellular matrix (ECM) in glial scars. Whether this holds equally true for reactive astrogliosis, a hallmark of MS, was not investigated.

However, MRE of the brain is not yet clinically established to date. This could be explained by a number of reasons. Contrary to liver elastography, no brain MRE examination setup is commercially available, posing a high entry threshold to institutions. As an evolving modality, hardware setup, acquisition parameters and post processing are still lacking standardization. Similarly, brain viscoelasticity data in literature is based on different methodology and is in part contradictory. Another aspect is that relative to conventional MRI, brain MRE's spatial resolution is still poor. Even though studies exploring regional stiffness properties do exist [60–63], most clinical studies have been conducted with respect to global brain viscoelasticity. Since global measures are likely to be confounded by various factors such as aging and sex [41, 64–66], their clinical significance is questionable.

These aspects highlight that MRE in brain is far from reaching its full potential. With recent advances in acquisition and processing techniques, MRE's role in investigation of neurological diseases has to be further evaluated.

1.5 Aims and Objectives

The aim of this thesis was to explore whether MRE can detect alterations in viscoelasticity in the *in vivo* MS brain and by that contribute to explaining the clinico-radiologic paradox. For this purpose, viscoelasticity measures were acquired in a controlled experiment and interpreted in the context of demographic, clinical and radiological characteristics. It was hypothesized that diffuse parenchymal brain damage is accompanied by a reduction in stiffness, which had been indicated in previous studies. It was further assumed that with progression of disease, reduction in stiffness is more pronounced.

In a between-cohort approach, the viscoelasticity of brain tissue in MS patients was compared with a healthy control group. This was done for WM, subcortical grey matter (SGM) and subregional regions of interest (ROIs). In patient-cohort analyses, viscoelasticity was put into context with lesion load, brain atrophy and clinical features. This study further investigated differences in stiffness between T2w lesions and NAWM due to their distinct pathological processes. In order to eliminate known and unknown confounding factors, analyses were performed with respect to individual spatial variations in brain stiffness. Although cortical alterations are of high interest in MS research, due to physical limitations in MRE imaging, this work did not examine cortical grey matter.

Finally, this thesis aimed to evaluate to what extent MRE meets the sensitivity and specificity required to complement paraclinical assessment of MS patients and if MRE can help understanding the underlying pathophysiology of MS.

2 Technical Background

2.1 Rheology

Rheology is the science that derives the elastic, viscous or viscoelastic properties of materials from studying their deformation (=strain) under mechanical stress [67].

The real world behavior of materials can be modelled by a combination of ideal rheological elements. A Hooke element is an ideal elastic body and often represented by a spring. Under stress, it instantaneously undergoes strain, that is proportional to the amount of stress in any moment. In the absence of stress, the original shape is completely recovered. A Newton element is an ideal viscous body and often represented by a springpot, which is a damper filled with a viscous fluid. Under stress, its deformation increases gradually over time. In the absence of stress, deformation persists [68].

All biological materials exhibit both viscous and elastic characteristics, which is why they are referred to as viscoelastic [69]. Rheological experiments aim at quantifying viscoelastic properties of materials, and ultimately can help to infer knowledge about the material's immanent structure. Static and dynamic experiments can be distinguished. A static method is indentation testing, which measures penetration depth at different loads. In biology, this method is routinely used *ex vivo* as well as *in vivo* in animal models. However, without invasive procedures, the use of indentation testing is limited.

2.1.1 Dynamic Oscillation Experiments

In a dynamic oscillation experiment, an object is subjected to periodic stress and relaxation in a sinusoidal manner. Subjected to sinusoidal shear stress, periodic shear waves will propagade through the material. In shear waves, adjacent slices perpendicular to the direction of wave propagation are displaced against each other, resulting in shear strain. Stress and strain curves can be plotted in a diagram over time (Figure 1).

The response of a purely elastic material (A) under sinusoidal stress is instantaneous, which is why stress and strain curves are in phase ($\varphi = 0$). In contrast, in a purely viscous material (C), response in strain is found a quarter of an oscillation period behind stress ($\varphi = \pi/2$). Consequently, in a viscoelastic material (B), φ ranges between 0 and $\pi/2$.

The viscoelasticity of a material under oscillatory conditions can be expressed using the complex shear modulus G^*. The magnitude $|G^*|$ (Pa) is the ratio of the absolute

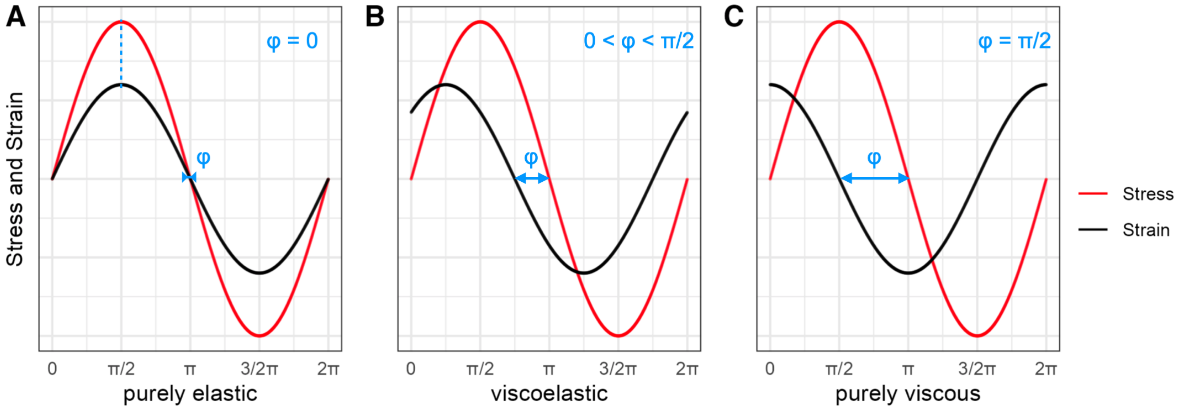

Figure 1: Stress and strain curves in elastic, viscous and viscoelastic materials

values of peak-to-peak stress to peak-to-peak strain. Low values correspond to a soft, high values to a stiff material. φ as the phase shift between stress and strain curves is the angle of G^* in polar form. In a material, it corresponds to the ratio of viscous to elastic properties with low values corresponding to a spring-like, high values to a fluid-like material.

It is important to note that $|G^*|$ and φ are two independent properties. E.g., an ideal spring is purely elastic ($\varphi = 0$), but can be made of thin or thick metal and by that is soft or stiff. Similarly, an ideal springpot is purely viscous ($\varphi = \pi/2$), but can be made of a fluid of low or high viscosity (such as water or honey, respectively) and by that is soft or stiff.

2.1.2 Viscoelasticity of Biological Soft Tissue

The microstructure of biological soft tissue is defined by a variety of elements, e.g., water, colloidal particles, ECM and intracellular filaments. The macrostructure is defined by its composition of parenchymal and connective elements as well as overall architecture. In organs, structural elements are heterogenously distributed and follow some degree of spatial alignment, which is why biological tissues are regarded as inhomogeneous and anisotropic [69]. Typical for soft tissue, the ratio of stress to strain is only constant for small stresses. This region is called linear viscoelastic region (LVER). When exceeded, a nonlinear response in strain is observed. This is evident as a strain-stiffening, which protects the tissue's integrity at larger deformations [70].

$|G^*|$ and φ are physical measures, whose translation into histological or structural correlates is complex and subject to current research. $|G^*|$ denotes the inherent adhesion or strength between structural building blocks in tissue. $|G^*|$ rises with an increase in connective elements per volume, such as collagen-1 deposition in the ECM [41, 58]. The angle φ is associated with the architecture or topology of tissue and is sensitive to the arrangement of building blocks [60, 71].

Subjected to manual palpation, adjacent layers of tissue undergo shear stress, leading to a tensed state of connective elements. This state counteracts further deformation, which can be perceived as stiffness. An increase in stiffness, e.g., in fibrosis, corresponds to an increase in connective elements and to a rise in $|G^*|$, which is why $|G^*|$ is the closest equivalent to a palpatory sensation [41, 72]. However, φ, representing the phase between stress and strain curves, can only be derived in dynamic viscoelasticity experiments.

2.2 Magnetic Resonance Elastography

In MRE, MRI is utilized to measure the displacement of tissue under stress. In a dynamic MRE experiment, mechanical waves are induced into the tissue of interest by coupling of an external sinusoidal oscillator. The resulting displacement of tissue is quantified by means of a motion-sensitive MRI sequence, yielding a displacement or wave map. Finally, by stiffness reconstruction algorithms, viscoelastic properties of tissue are estimated at different points in space [73].

2.2.1 Motion Encoding

In an MRI scanner, spins of protons are precessing around the main magnetic field axis z. After excitation by a defined radiofrequency pulse, spins are tipped into the transverse plane xy. Thereby, spins are brought into phase. As individual tiny magnets, in phase, spins add up to a net transverse magnetization vector M_{xy}, whose magnitude and phase can be measured as a signal by receiving coils.

In MRE, motion-sensitive sequences induce a change in phase for moving spins by motion encoding gradients (MEGs). A magnetic gradient alters the strength of the magnetic field to a unique value at each point along its axis. The MEG is a bipolar gradient, which can be separated into two sequential halves with opposite polarity but identical magnitude. Subjected to the positive half of the gradient, a spin is gaining phase. In the case of a stationary spin, the negative half reverses this gain in phase completely. In contrast, a moving spin is subjected to both halves of the MEG at different locations, which is why its phase change is not reversed. As a result, a net phase shift remains.

In elastography, spin movement is induced by shear waves propagading through tissue. As a consequence, tissue displacement is encoded in the phase of the vector M_{xy}, which can be measured by phase-sensitive MRI sequences. Figure 2 depicts the difference in phase between moving and stationary spins subjected to MEGs.

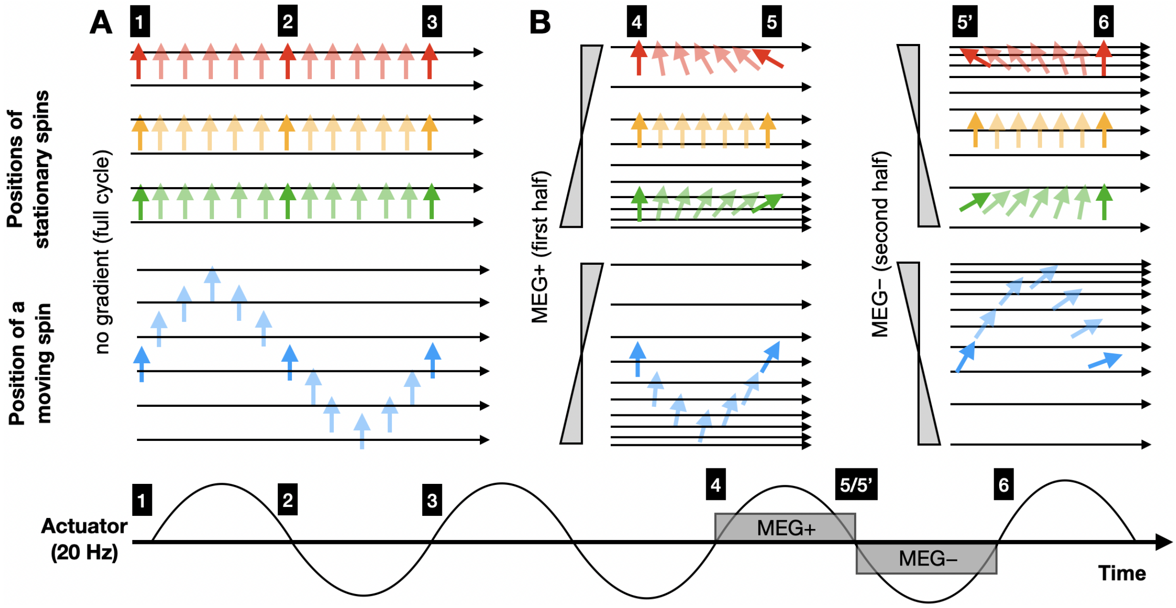

Figure 2: Phase between stationary and moving spins during motion encoding. Motion encoding is accomplished using a bipolar gradient. Red, yellow and green are stationary spins, blue is a moving spin. When there is no gradient present (A), no phase shift is happening to all spins (time points 1-3). Then a bipolar MEG is applied (4-6) with its positive part (MEG+) between 4 and 5 and its negative part (MEG−) between 5' and 6. The magnetic field is altered along its axis, illustrated by narrowing or widening of magnetic field lines. In the case of stationary spins (red/yellow/green), a phase shift acquired between 4-5 is fully reversed at 6. Contrary to that, phase shift of the moving spin (blue) is not reversed.

2.2.2 Wave Image Acquisition

A spin's phase shift carries movement information cumulated during the spin's exposure to the MEG. That is why multiple displacement readouts within one oscillation period are desired to obtain a complete time-resolved wave picture [37]. Furthermore, in order to obtain a full displacement field in space, MEGs have to be consecutively applied in three spatial dimensions.

As an analogy, in electrocardiography, the direction and magnitude of the electrical heart vector can only be obtained by probing it with leads from different directions. This is done many times per heart cycle, revealing the vector's temporal course. In motion encoding, typically, a time series of four snapshots within the actuator's wave period is recorded, for which MEGs are manipulated in length and phase offset relative to a wave period. By Fourier transformation, this time series is brought from time into frequency space, ultimately yielding a wave image.

2.2.3 Reconstruction of Viscoelastic Properties

Based on the acquired wave field, the underlying viscoelastic properties of tissue need to be reconstructed. Mathematically, the deduction of causal parameters based on an object's observed behavior is referred to as an inverse problem [74]. Depending on the inversion algorithm, various assumptions about tissue properties including linearity, homogenity, isotropy and compressibility have to be made, which is why various mathematical approaches with specific advantages and disadvantages exist [75–77]. One key concept of inversion algorithms is that waves propagade slower in soft and faster in stiff regions, resulting in different regional wave lengths at a constant actuation frequency (Figure 3). The reconstructed spatial map of viscoelasticity data is often referred to as stiffness map or elastogram. However, strictly speaking, these terms only reflect the $|G^{*}|$ part of the viscoelasticity map, which is why they are not used in this thesis.

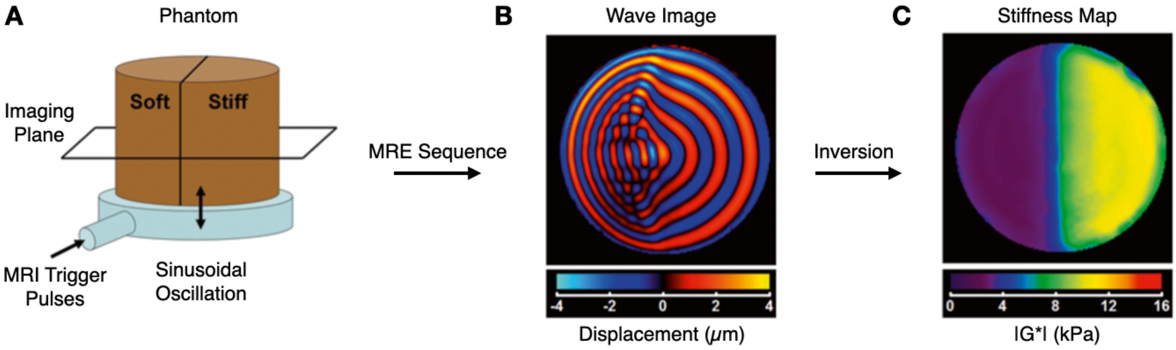

Figure 3: Viscoelasticity reconstruction by inversion. A phantom (A) with a soft and stiff half is mechanically excited by a sinusoidally moving membrane, which is synchronized to the MRI scanner by trigger pulses. By means of an MRE sequence, a displacement map can be calculated, depicted as a cross-sectional wave image (B). Reflecting regional stiffness variations in the phantom, wave lengths are shorter (soft) or longer (stiff). Finally, inversion algorithms translate the wave image into a map of viscoelasticity parameters. Illustration adapted from Venkatesh et al. [27, p. 21].

3 Material and Methods

This study was designed as a controlled study of one hundred patients with diagnosed MS and an equal number of healthy volunteers as controls. In the following, these groups are referred to as MS and healthy control (HC) cohorts. The terms *participants* and *subjects* encompass both cohorts. The study was approved by the local ethics committee.

3.1 Participants

3.1.1 Recruitment and Assessment

Examination of participants started in autumn 2019. All participants gave written informed consent. Each participant underwent a single MRI examination according to the study protocol. Inclusion criteria were age greater than 18 years and absence of MRI contraindications. In the HC cohort, absence of known neurological or psychiatric diseases in the healthy volunteers' medical history was mandatory. Inclusion criteria for the patient cohort were diagnosis of MS according to 2017 McDonald criteria [6] or CIS suggestive of MS [3]. Disability was quantified using the Expanded Disability Status Scale (EDSS) [11].

Date of birth and sex were collected from all participants. In patients, following clinical data were gathered: disease duration, EDSS score and date, MS therapy and MS phenotype. Disease duration was defined as difference between date of first symptoms related to MS and date of MRI examination. MS therapy and phenotype data refer to date of EDSS assessment. Clinical assessment and MRI examination were performed in a period without relapse in a stable state of disease, defined as a minimum of eight weeks since last symptoms and last drug intake related to relapse. Clinical assessment was conducted by experienced clinicians at the MS outpatient department of the Medical University of Graz in a patient's routine ambulatory visit. Clinical data were extracted retrospectively from the patient research database. In case of multiple clinical records around MRI date, the assessment date closest to MRI examination was chosen.

3.1.2 Demographic and Clinical Data

At the time of writing this thesis, 73 MS and 42 HC subjects were examined. Ratio of males to females was 25:45 in the MS cohort and 21:21 in the HC cohort, respectively.

However, two patients underwent scanning during a relapsing phase. Furthermore, in one patient, diagnosis of MS was questionable due to atypical image findings. Therefore, the total number of patients meeting inclusion criteria was reduced to 70. Age distribution of both cohorts is shown in Figure 4.

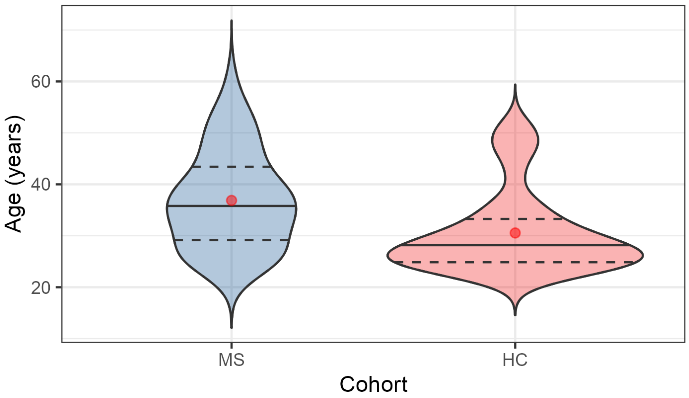

Figure 4: Age distribution of participants on scan date. In each violin plot, the solid line depicts the median, the red dot represents the mean, and dashed lines show lower und upper quartiles.

MS phenotype count of CIS/RRMS/SPMS/PPMS was 15/51/4/0. Due to poor representation of progressive MS phenotypes, no distinction was made concerning MS phenotype in statistical analyses. EDSS distribution is depicted in Figure 5. Median EDSS was 1.5 (range 0 to 5.5, IQR 2.25). Based on the median, for further analysis, two subgroups *EDSS low* (≤1.5) and *EDSS high* (>1.5) were defined. Mean time difference in days between EDSS assessment and MRI examination was 1 (±80).

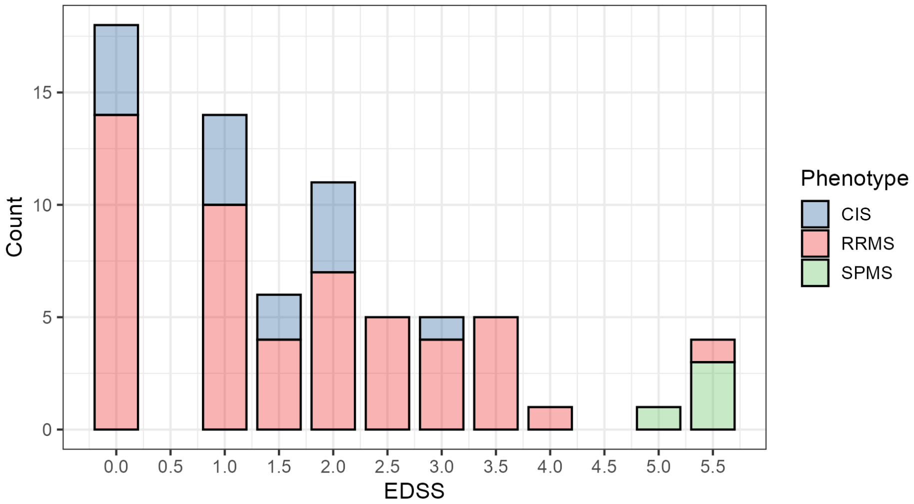

Figure 5: Distribution of EDSS scores in the MS cohort

Demographic data of both cohorts as well as clinical data for the MS cohort are shown in Table 1.

	MS (all)	EDSS ≤1.5	EDSS >1.5	HC
Demographic data				
N total (male:female)	70 (25:45)	38 (11:27)	32 (14:18)	42 (21:21)
Age in years	36 (14.25)	38.5 (16.5)	34 (11.5)	28 (7.75)
male	38 (16)	42 (19.25)	34 (13)	29 (8)
female	35 (12)	37 (16.75)	34 (10.5)	26 (5)
Clinical data				
Disease duration in years	7 (8.75)	5.5 (7)	9.5 (10)	
CIS/RRMS/SPMS count	15/51/4	10/28/0	5/23/4	
DMT count	44	27	18	

Table 1: Demographic and clinical data of participants. Age and disease duration data represent median (IQR). In the MS cohort, there further was distinguished between subgroups EDSS low/high.

3.2 Examination Setup

Each subject's head was resting on a head rocker and fixated by foam paddings to achieve mechanical coupling. The head rocker is limiting head motion to a nodding motion. A piezoceramic actuator (SPL Spindel und Präzisionslager GmbH, Ebersbach, Germany) paired with a high-power wave generator (CGC Instruments, Chemnitz, Germany) was used to create a continuous sinusoidal push/pull motion. The actuator was located at the end of the subject's table to avoid magnetic field disturbances. The actuator was connected to the head rocker with a rigid carbon rod, thus introducing mechanical shear waves inside the skull (Figure 6).

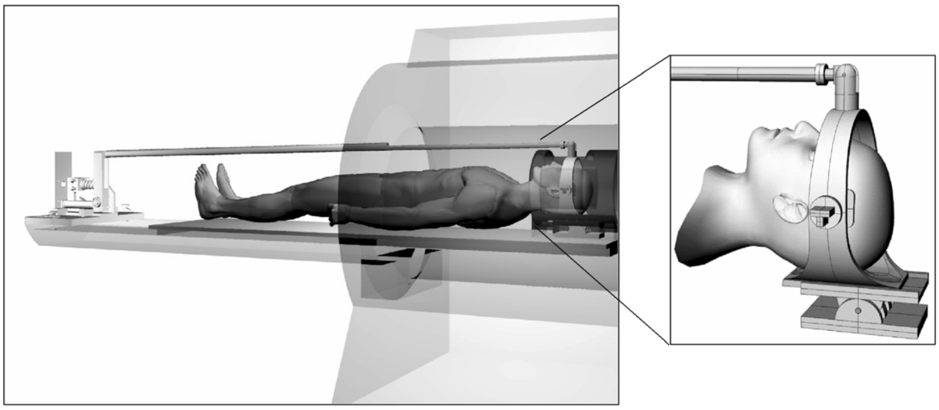

Figure 6: MRE examination setup. A piezoceramic actuator was connected to a head rocker with a carbon rod. Illustration from Streitberger et al. [78].

3.3 Image Acquisition

All experiments were carried out on a SIEMENS Prisma 3T whole-body MR scanner (Siemens Healthcare, Erlangen, Germany) with a 20-channel head coil. Both cohorts underwent identical protocols, starting with the MRE sequence and followed by T1w and T2w sequences. Structural T1w and T2w images were acquired for the purpose of co-registration of the MRE images, segmentation of CSF and parenchymal structures, brain volumetry and MS lesion detection. Before image acquisition, a localizer sequence was run to define the field of view (FOV) and adjust the anterior-posterior axis parallel to the corpus callosum.

Throughout MRE image acquisition, mechanical actuation was synchronized with the MRE sequence through trigger events. Actuation was started before image acquisition in order to establish a steady state shear field before initiation of the motion encoding sequence.

Sequence Parameters

Image acquisition parameters are depicted in Table 2. For T1w imaging, a 3D gradient echo inversion recovery sequence was used (3D-MPRAGE) [79, 80]. Lesion delineation was accomplished by T2w imaging with a 3D fluid-attenuated inversion recovery sequence (3D-SPACE-FLAIR) [81]. No contrast-enhancing agents were applied. Identical parameters for slice number, base resolution and voxel size were chosen for both structural imaging modalities.

Parameter	3D-MPRAGE	3D-SPACE-FLAIR	Multiphase DENSE
Base resolution In-plane	256 × 256	256 × 256	300 × 300
Slices	176	176	25
In-plane resolution (mm)	1 × 1	1 × 1	2.34 × 2.34
Slice thickness (mm)	1	1	4
FOV (mm)	224 × 256	256 × 256	300 × 300
TR/TE/TI (ms)	1900/2.7/900	5000/393/1800	2500/7.6/–
Flip Angle α (deg)	9	variable	30/35/45/90
Orientation	sagittal	sagittal	transversal
Acquisition Time (mm:ss)	06:01	04:25	07:30
Mixing Times TM_{1-4} (ms)			8/20.5/33/45.5
Actuation frequency (Hz)			20

Table 2: T1w, T2w and MRE imaging acquisition parameters. FOV = field of view; TR = time to repetition; TE = time to echo; TI = time to inversion; TM = mixing time.

Motion encoding was performed with a multiphase DENSE (displacement encoding with stimulated echoes) sequence at an actuation frequency of 20 Hz. DENSE is a motion-sensitive sequence, which facilitates a high signal-to-noise ratio (SNR) at low actuation frequencies [82, 83]. Low-frequency actuation provides high tissue penetration depth, which is suitable for brain elastography. In DENSE, stimulated echoes encode displacement information into the longitudinal magnetization M_z of spins. Contrary to the transverse magnetization M_{xy}, phase information in M_z is robust to free induction decay (FID) [84]. Moreover, motion-encoding can be separated from data readout, which is why TE can be short at low actuation frequencies, resulting in a better SNR.

In MRE, a series of images with different phase offsets relative to mechanical excitation must be recorded in order to sample time-resolved displacement data. In this study, a multiphase DENSE sequence was used, which was first proposed by Strasser et al. [85] in 2019 and successfully tested in phantoms as well as healthy volunteers. Multiphase

DENSE facilitates a readout of displacement data at multiple phase offsets during one time to repetition (TR), designated as mixing times TM_{1-4} (Table 2).

With a FOV of 300 × 300 mm and a matrix size of 128 × 128, a spatial resolution of 2.3 × 2.3 mm in plane at 4 mm slice thickness was achieved. Acquisition time per spatial dimension was 2 min 30 sec, totalling 7 min 30 sec.

3.4 Post Processing

After wave image calculation, background phase was subtracted and images were smoothed with a 2D Gaussian filter (5 × 5 pixel kernel, $\sigma = 1$). Wave inversion was performed using a multi-frequency dual elasto-visco (MDEV) inversion algorithm, assuming a homogenous brain density of 1 g/cm^3 [86]. MDEV has proven robust results in numerous studies [78, 87]. Displacement information and binary brain masks were supplied to MDEV, thereby reconstructing magnitude $|G^*|$ and phase angle φ of the complex shear modulus. T2w FLAIR images and maps of $|G^*|$ and φ were co-registered to T1 by affine transformation, which comprises translate, scale, rotate and shear transformations. For better readability, in the following, used software commands and parameters are written in `monospace` font.

3.5 Segmentation and Masking

3.5.1 Segmentation

For each participant, segmentation of WM and SGM was performed on the original T1w image with the FreeSurfer image analysis suite in version 7.1.1 [88].

Lesion segmentation was done using the untrained Lesion Prediction Algorithm (LPA) of the Lesion Segmentation Toolbox version 3.0.0 (LST) [89], further referred to as LST-LPA. The software was run as a toolbox inside SPM12 (Statistical Parameter Mapping, build version 7771, University College London, London, UK) in MATLAB 2019a [90]. LPA was supplied with co-registered FLAIR images as input data without additional reference images. Next, lesion filling of the original T1w image was performed in LST by applying LPA's propabilistic lesion maps [91, 92].

Segmentation of cortical and ventricular cerebrospinal fluid (CSF) was achieved using SPM12 in a 1-channel approach with the original T1w image in the HC cohort and lesion-filled T1w image in the MS cohort, respectively. All default settings were maintained. CSF probability maps were liberally thresholded with 0.75 (`fslmaths -thr 0.75 -bin`) and binarized. Segmentation of WM, WM subregions and SGM subregions was performed in FreeSurfer as part of the `recon-all` analysis pipeline according to labels presented in Table 3.

For subsequent `FSL` analysis, segmentation results were transformed from FreeSurfer back to native space (`mri_label2vol` with `rawavg.mgz` as a target file).

ROI	Left Hemisphere		Right Hemisphere	
	ID	Label	ID	Label
WM	2	Left-Cerebral-White-Matter	41	Right-Cerebral-White-Matter
	(78)	(Left-WM-hypointensities)	(79)	(Right-WM-hypointensities)
frontal lobe	3201	wm-lh-frontal-lobe	4201	wm-rh-frontal-lobe
occipital lobe	3204	wm-lh-occipital-lobe	4204	wm-rh-occipital-lobe
temporal lobe	3205	wm-lh-temporal-lobe	4205	wm-rh-temporal-lobe
parietal lobe	3206	wm-lh-parietal-lobe	4206	wm-rh-parietal-lobe
insula lobe	3207	wm-lh-insula-lobe	4207	wm-rh-insula-lobe
SGM	10-13	*see below*	49-52	*see below*
thalamus	10	Left-Thalamus-Proper	49	Right-Thalamus-Proper
caudate	11	Left-Caudate	50	Right-Caudate
putamen	12	Left-Putamen	51	Right-Putamen
pallidum	13	Left-Pallidum	52	Right-Pallidum

Table 3: FreeSurfer labels list for binary mask creation. Labels denoted in brackets were only respected in patients.

3.5.1.1 White Matter Subregions

WM was segmented into the following lobar structures, defining 5 subregional ROIs: frontal, insular, temporal, parietal and occipital. Labels were chosen according to FreeSurfer's label lookup table as presented in Table 3.

Lobar parcellation was performed based on FreeSurfer's cortical parcellation as output in the `aparc` file. Cortical parcellation was extracted with the `mri_annotation2label` program, which was supplied with the `--lobesStrict` parameter. Lobe labels were then projected onto the WM volume using `mri_aparc2aseg` with the parameters `--labelwm`, `--hypo-as-wm` and `--rip-unknown`. In order to avoid missing major parts of the WM, the projection volume was expanded by setting the `--wmparc-dmax` parameter to 100. Finally, parcellated volumes were brought into native space as mentioned above and converted to the NIfTI format [93].

3.5.1.2 Subcortical Grey Matter Subregions

In this thesis, SGM is defined as the sum of the following subregions: thalamus, putamen, caudate nucleus and pallidum. Amygdala and hypothalamus are not part of this work's analyses due to incomplete FOV coverage as well as questionable viscoelasticity measures in proximity to the base of skull. In accordance with WM parcellation, labels were brought into native space and converted to the NIfTI format. Subregions were chosen as depicted in Table 3.

All subregion masks included both hemispheres. After each process, all results were inspected visually. No manual changes were made.

3.5.2 Binary Mask Creation

In all subjects, binary masks for ROIs WM, subregions of WM and subregions of SGM were created based on FreeSurfer's segmentation results as shown above. All further calculations were performed with various tools from the FMRIB Software Library (FSL) in version 6.0.0 [94–96].

In order to account for segmentation inaccuracy of WM in the region of MS lesions, in the patient group, additional steps were performed. Lesion probability maps obtained by LST-LPA, liberally thresholded with 0.9, as well as FreeSurfer's WM hypointensity masks (labels 78 and 79) were added to FreeSurfer's WM segmentation, resulting in robust WM masks for the MS cohort. Consequently, NAWM masks were obtained by subtraction of lesion probability maps, thresholded with 0.25, from WM masks.

3.5.2.1 Cerebrospinal Fluid Distance Filtering

The validity of stiffness measurements in voxels close to impedance leaps, most notably through surrounding CSF, is questionable. That is why distance maps were calculated with respect to the CSF masks obtained by SPM12 segmentation. Given a theoretical MRE resolution of 2.34 mm, the distance mask was thresholded with 3 mm, eliminating measurements within 3 mm to the CSF. The process of segmentation, mask calculation and distance filtering is illustrated in Figure 7.

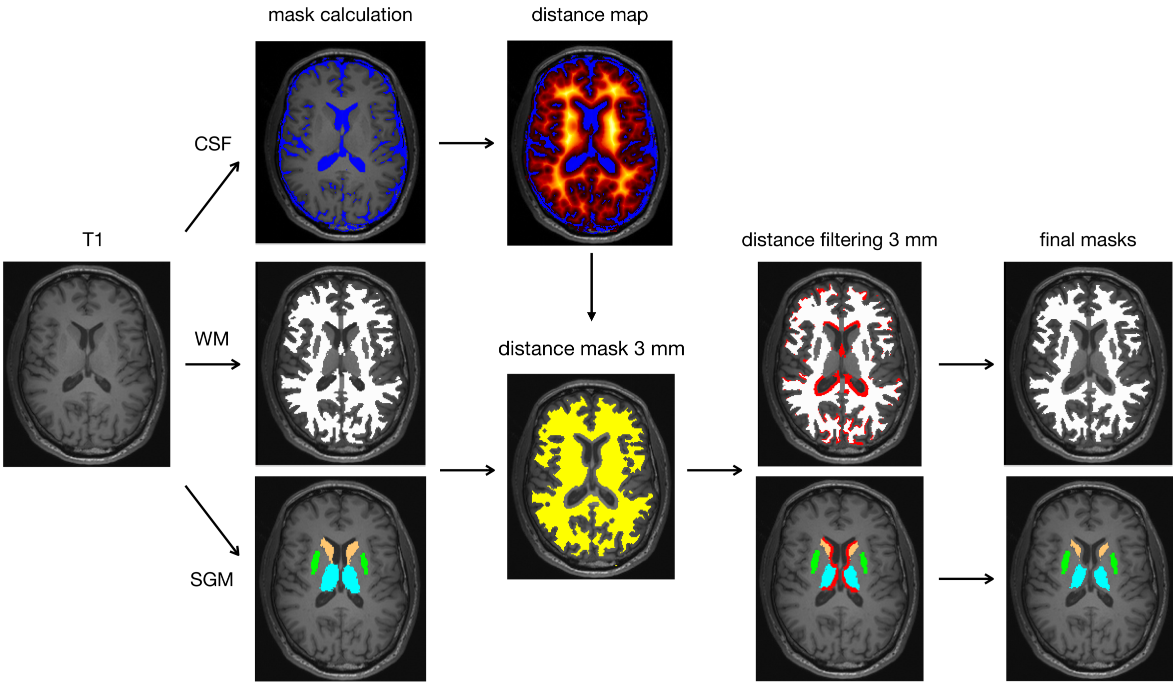

Figure 7: Mask calculation pathways for WM and SGM

3.5.2.2 Lesion Mask Creation

For lesion analysis, probabilistic lesion maps obtained by LST-LPA were binarized with a conservative threshold of 0.25, further referred to as lesion mask. According to Weeda et al. [97], 0.25 has shown to be the optimal probability threshold with LST-LPA.

However, especially in small lesions, it can be assumed that MRE voxel values are significantly affected by noise from surrounding structures. Therefore, a three-dimensional cluster analysis on connecting voxels was performed on the lesion mask, approximating the volume of individual lesions. Only lesions with a minimal volume of $50\,\mathrm{mm}^3$ were included for stiffness analyses. No discrimination concerning lesion shape and position was made.

In contrast, for lesion load calculation, all lesions in the T2w FLAIR FOV with a minimal volume of $10\,\mathrm{mm}^3$ were included and summed. Volume calculation was done with `fslstats -V`.

3.6 Image Data Analyses

3.6.1 Lesions and Normal-Appearing White Matter

It is known from the literature that viscoelasticity in healthy WM exhibits characteristic regional variations, e.g., a higher stiffness around the poles [98]. As a consequence, mere analysis of mean stiffness values across all lesions can disguise significant alterations in lesion viscoelasticity relative to NAWM. In order to account for this, three individual analysis pathways were performed as shown in Figure 8.

A) Comparison with contralateral NAWM In a within-subject voxel-wise approach, lesion stiffness was referenced to NAWM in the corresponding region of the contralateral hemisphere. A corresponding region was defined as a mirrored point along x-axis in MNI152 space. Therefore, lesion masks and stiffness maps were transformed into MNI152 space as described in subsection 3.6.3. However, in lesions symmetrically present in both hemispheres, a mirrored lesion voxel does not coincide with contralateral NAWM and therefore was not included in further analysis. In order to exclude contralateral NAWM adjacent to lesions, before mirroring, the lesion mask was enlarged by Gaussian blur (`fslmaths <in> -s 2 -thr .05 -bin <out>`), demanding a lesion-free margin of approximately 2 mm thickness in the contralateral NAWM.

B) Comparison with surrounding NAWM Secondly, lesion stiffness was related to the immediate surrounding NAWM. This was accomplished by creating a margin around the lesions with Gaussian blur (`fslmaths <in> -s 2 -thr .05 -bin <out>`) and consecutive subtraction of the lesion mask. The resulting mask was subsequently masked with the distance-filtered NAWM, thus avoiding expansion into non-NAWM regions.

C) Comparison with healthy WM Finally, lesion stiffness was related to corresponding healthy WM regions. Therefore, all viscoelasticity maps of the HC cohort were transformed into MNI152 space and voxel-wise averaged. Global lesion masks in MNI152 space were then projected on averaged healthy WM. Conversion pipeline to MNI152 space is presented in subsection 3.6.3.

3.6.2 Brain Atrophy Estimation

SIENAX, part of FSL, was used to estimate normalized brain volume (NBV) as a surrogate for brain atrophy [94, 99]. Based on skull size, SIENAX is accounting for physiological brain volume variability. By determining a scaling factor between a subject's brain volume and standard space, normalized volumes for the brain and subregions are calculated.

Beforehand, neck-stripping was applied with `robustfov`. SIENAX was then supplied with the neck-stripped T1w image in the HC cohort and neck-stripped lesion-filled T1w image in the MS cohort, respectively. SIENAX calls a number of analysis subprogrammes: in a first step, BET is utilized for extraction of brain and skull. SIENAX was supplied with the parameters `-r -B -f 0.35`. Passing BET a fractional intensity threshold of 0.35 yielded consistent brain segmentation results in all subjects. With the `-r` parameter, normalized volumes were calculated for WM, total GM and peripheral cortical GM. In order to approach SGM atrophy, the normalized peripheral cortex volume was subtracted from the normalized GM volume.

3.6.3 Registration to MNI152 Space

Mapping of brain scans into a standardized coordinate system is a prerequisite for voxel-wise between-subject analyses. MNI152 is an anatomical template image common in neuroimaging, which was derived as an average of 152 structural T1w scans. Transformation into MNI152 space was done in order to facilitate lesion mirroring, visual data inspection and comparison across studies.

A transformation matrix was calculated with FSL on the T1w image of each participant. The image was first affine transformed using `flirt` with a $1\,\mathrm{mm}^3$ voxel MNI152 reference and `corratio` as cost function. Subsequently, the image was warped with `fnirt --subsamp=8,4,2,2`. Finally, the resulting transformation matrix was applied on $|G^*|$ and φ maps with `applywarp`. In case of transformation of binary masks, transformations were thresholded with 0.5.

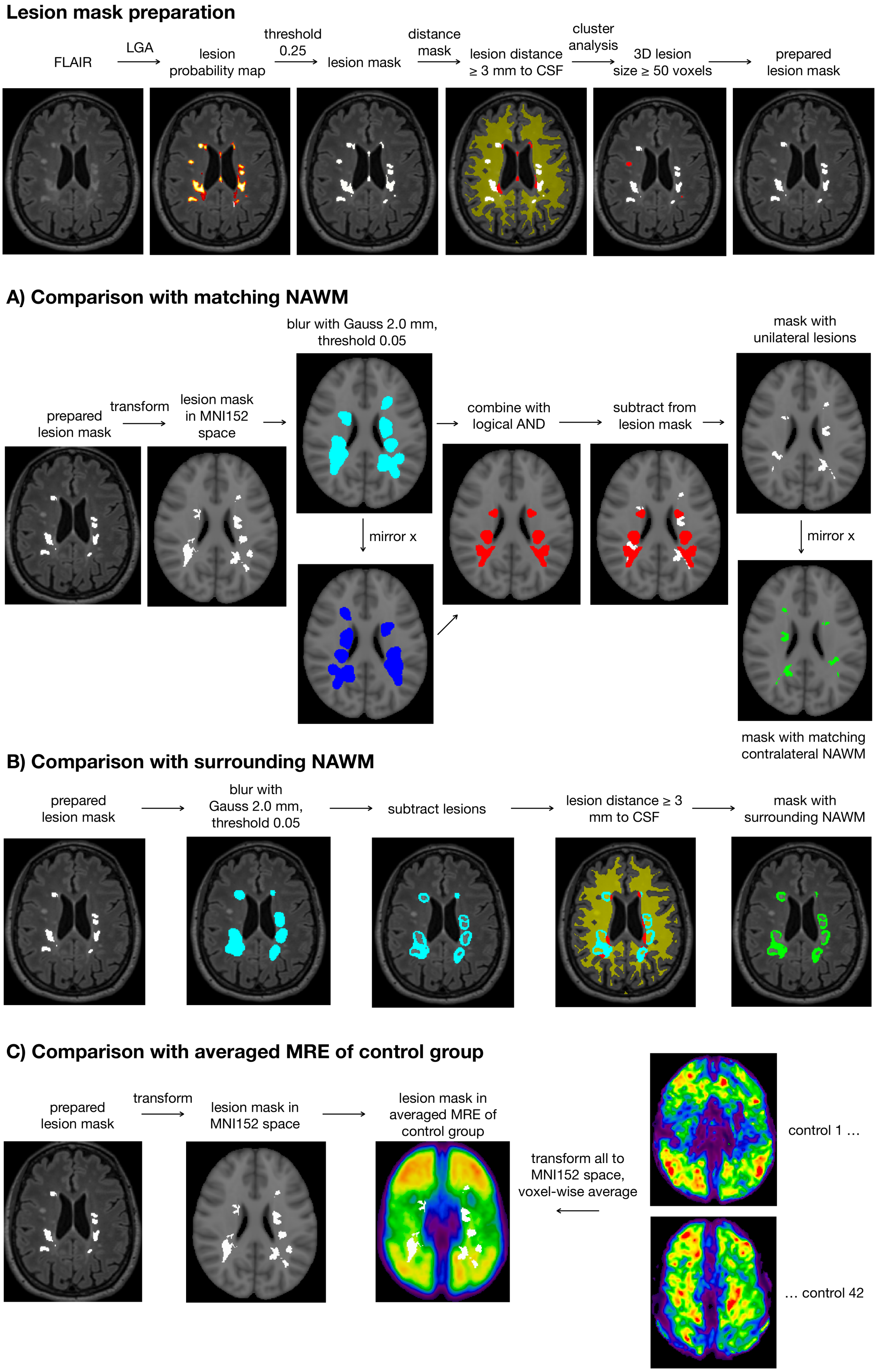

Figure 8: Lesion mask preparation and analysis pathways

3.7 Statistical Analyses

For statistical analyses and data visualization, R in version 4.0.5 was used. Data distribution is depicted by box-and-whisker plots with the box representing the median and its hinges representing the 25th percentile (Q_1) and 75th percentile (Q_3) [100]. The upper whisker depicts the largest observation less than or equal to $Q_1 - 1.5 \times IQR$ ($IQR = Q_3 - Q_1$). The lower whisker represents the smallest observation greater than or equal to $Q_3 + 1.5 \times IQR$, respectively. Observations exceeding whiskers were defined as outliners and denoted as dots.

A significance level $\alpha = 0.05$ was set for all statistical tests. Normality was assessed with the Shapiro-Wilk normality test prior to all analyses. Parametric tests were used for all inductive statistics when normality could be assumed. Two-tailed Student's t-tests and Pearson's correlations were performed for parametric data. Wilcoxon signed-rank tests and Spearman's rank correlations were used for non-parametric data. In tables, significant results are highlighted in bold. The term *significant* always refers to statistical significance.

Brain maps of the complex shear modulus G^* were obtained for each participant. Statistical analyses were separately performed on the magnitude $|G^*|$ and phase angle φ of G^*. Therefore, the use of G^* in context of statistical evaluation always refers to separate analysis of $|G^*|$ and φ.

Statistical image analyses were performed with `fslstats` as part of FSL. For each subject, means of $|G^*|$ and φ were calculated with the `-M` parameter within various ROIs. This was done by applying binary masks as calculated above to whole-cerebral maps of $|G^*|$ and φ. Each calculated mean was further considered as one single observation – thus, presented values for $|G^*|$ or φ within a ROI in a subject are always representing the mean voxel value within that ROI. Consequentially, a denoted summary statistic describing a set of observations is in fact reporting a set of mean voxel values. Measures of $|G^*|$ or φ within a given ROI are also denoted as $|G^*|_{ROI}$ or φ_{ROI}, respectively. Both $|G^*|$ and φ were considered to be at least interval scaled. Units for $|G^*|$ and φ are consistently tabulated in *Pa* and *rad*, respectively. Unless otherwise stated, ROIs always encompass both hemispheres.

4 Results

Viscoelasticity data presentation and statistics are arranged as follows: Firstly, data were visualized as viscoelasticity maps. Secondly, in intra-cohort analyses, G^* was put into context with sex, age and regional brain atrophy. Thereafter, G^* was related to patient-specific clinical and radiological findings, namely disease duration, EDSS and lesion load and compared between T2w lesions and NAWM. Finally, ROI-based comparison of MRE data was performed for WM, SGM and subregions between cohorts.

According to Table 4, normality was assumed for G^* in WM and SGM in both cohorts.

G^*	Cohort	WM	SGM
$\|G^*\|$	MS	$W = 0.99$, $p = 0.58$	$W = 0.99$, $p = 0.84$
	HC	$W = 0.97$, $p = 0.41$	$W = 0.97$, $p = 0.35$
φ	MS	$W = 0.98$, $p = 0.46$	$W = 0.99$, $p = 0.72$
	HC	$W = 0.99$, $p = 0.86$	$W = 0.98$, $p = 0.82$

Table 4: Shapiro-Wilk normality tests for G^* in WM and SGM

4.1 Viscoelasticity Map Visualization

Maps of within-cohort averages and between-cohort differences of $|G^*|$ and φ are presented in Figure 9. Slices indicated a symmetrical distribution of viscoelasticity between hemispheres. Patterns of $|G^*|$ and φ suggested independence of both parameters.

Generally, visual inspection of maps of $|G^*|$ and φ revealed no direct relation to anatomical structures. High values for $|G^*|$ were found in the frontal, occipital and parietal lobes as well as the putamen. Low values for $|G^*|$ dominated in deep brain structures. Although a reduced $|G^*|$ could be assumed in SGM, there was no clear separation between WM and subcortical or cortical GM. The difference map $\Delta|G^*|$ indicated a diffuse reduction in stiffness (red) in the MS cohort, most prominently in levels above the lateral ventricles. In the $\Delta\varphi$ map, no general trend was observed between cohorts. However, a diffuse increase in φ was observed in SGM and the dorsal region in patients.

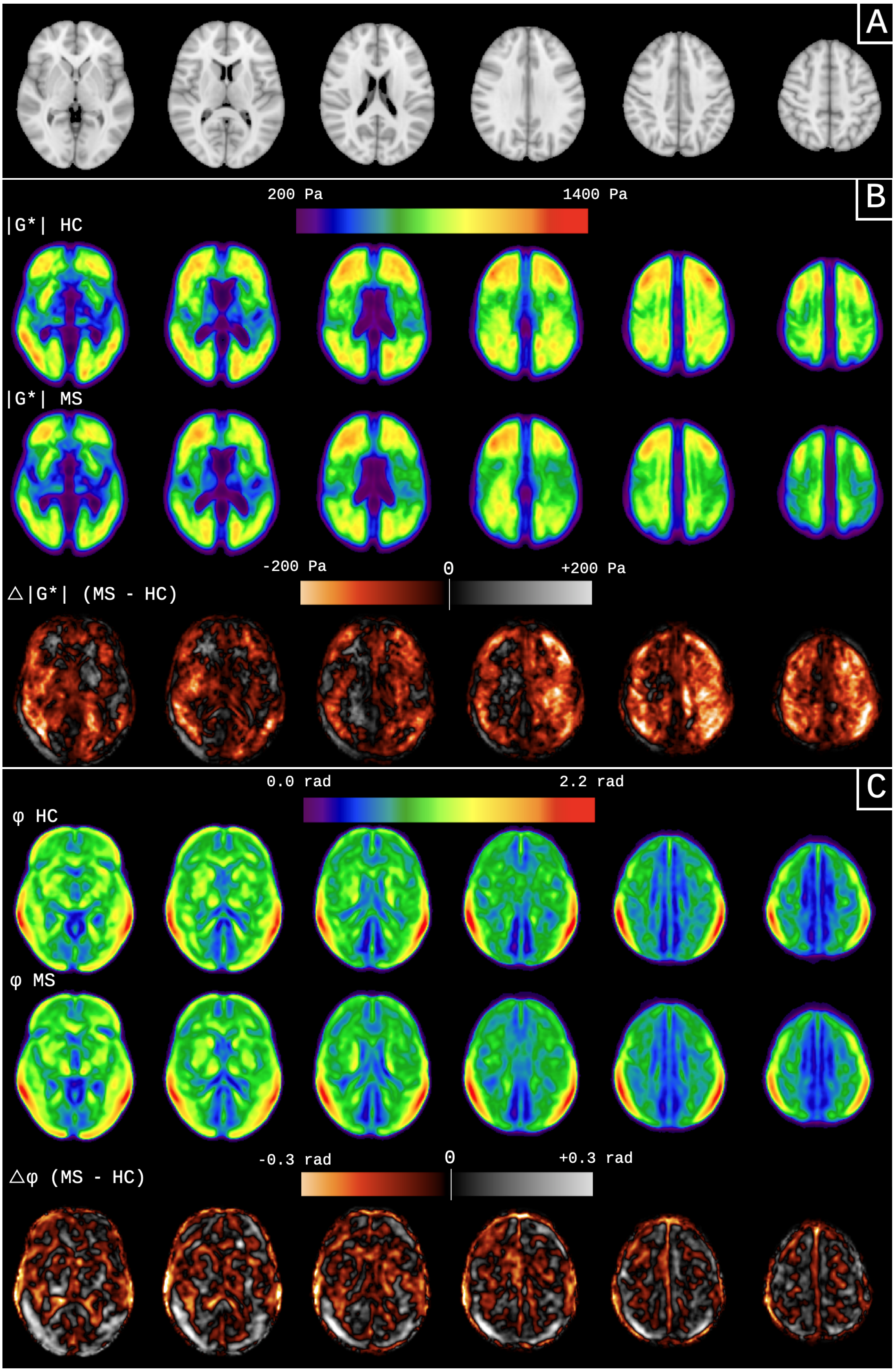

Figure 9: Visualization of voxel-wise averages in MNI152 space. (A) depicts the T1w MNI152 template image for anatomical reference. (B) and (C) depict maps of within-cohort averages of $|G^*|$ and φ after transformation into MNI152 space. Maps were color-coded with a window of 200 to 1400 Pa for $|G^*|$ and 0 to 2.2 rad for φ. Difference maps $\Delta|G^*|$ and $\Delta\varphi$ depict voxel-wise subtraction of cohort averages. Z-range: -5 to $+60$ (world coordinates) with a slice spacing of 10 mm for all images.

4.2 Intra-Cohort Analyses

A detailed description of demographic and clinical characteristics of participants can be found in subsection 3.1.2.

4.2.1 Sex

This study observed a sexual dimorphism with increased brain viscoelasticity in females ($|G^*|$: $p = 0.001$; φ: $p < 0.001$) (Figure 10). Cohort- and ROI-based analyses are tabulated in Table 5. No inter-cohort difference in effect strength was discernible.

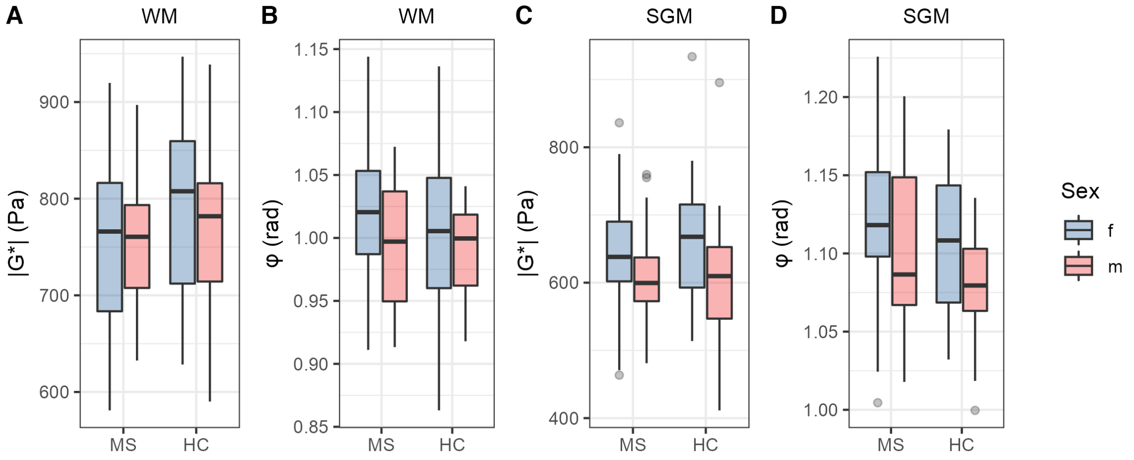

Figure 10: Distribution of G^* according to sex. Boxplots representing the distribution of $|G^*|$ (A, C) and φ (B, D) in WM and SGM of males (m) and females (f) in MS and HC cohorts.

		WM				SGM			
G^*	Cohort	Mean±SD females	Mean±SD males	Δ	Student's t	Mean±SD females	Mean±SD males	Δ	Student's t
$\lvert G^*\rvert$	MS	756 ± 79	751 ± 70	1%	$t = 0.27$, $p = 0.79$	641 ± 77	610 ± 67	5%	$t = 1.68$, $p = 0.10$
	HC	785 ± 91	764 ± 86	3%	$t = 0.75$, $p = 0.46$	666 ± 101	604 ± 104	10%	$t = 1.97$, $p = 0.06$
φ	MS	1.02 ± 0.05	0.99 ± 0.05	3%	$t = 2.44$, $p =$ **0.02**	1.12 ± 0.04	1.10 ± 0.05	2%	$t = 1.87$, $p = 0.06$
	HC	1.01 ± 0.07	0.99 ± 0.04	2%	$t = 0.89$, $p = 0.38$	1.11 ± 0.04	1.08 ± 0.04	3%	$t = 2.17$, $p =$ **0.04**

Table 5: Descriptive statistics of G^* in females and males as well as Student's t-tests for sex-related differences in G^*. Units for $|G^*|$ in *Pa*, φ in *rad*. Δ depicts percental differences between means.

4.2.2 Age

Age was not normally distributed in both cohorts (MS: $p = 0.01$; HC: $p < 0.001$). In the MS cohort, age was significantly higher ($p < 0.001$). Data suggested no age-dependency of G^* in WM (Figure 11). In SGM, an age-dependent reduction in φ was observed, which was significant in patients (MS: $\rho = -0.38$, $p = 0.002$) (Table 6).

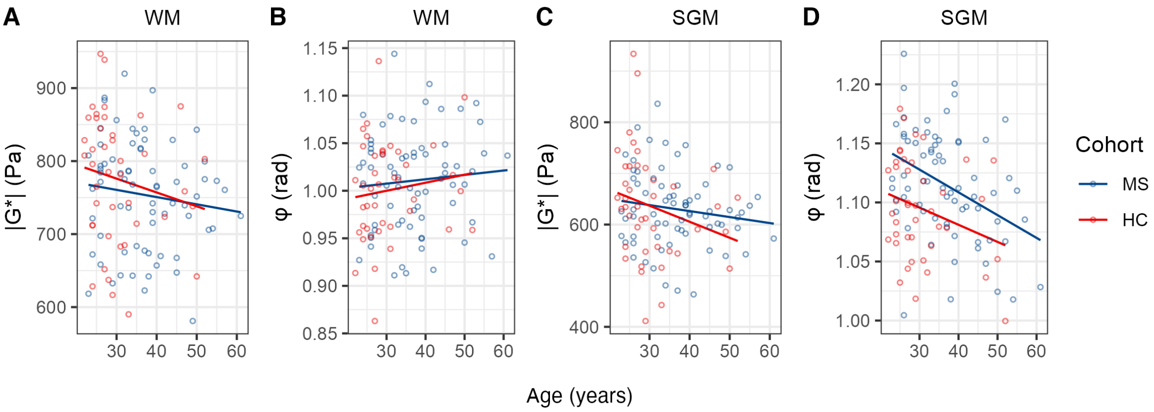

Figure 11: $|G^*|$ (A, C) and φ (B, D) in WM and SGM as functions of age.

G^*	Cohort	WM	SGM
$\lvert G^*\rvert$	MS	$\rho = -0.15$, $p = 0.21$	$\rho = -0.12$, $p = 0.34$
	HC	$\rho = -0.24$, $p = 0.13$	$\rho = -0.37$, $p = \mathbf{0.02}$
φ	MS	$\rho = +0.07$, $p = 0.59$	$\rho = -0.38$, $p = \mathbf{0.002}$
	HC	$\rho = +0.17$, $p = 0.29$	$\rho = -0.21$, $p = 0.18$

Table 6: Spearman's rank correlations between age and G^*

4.2.3 Regional Atrophy

Distributions of normalized volume estimates for WM (NV_{WM}) and SGM (NV_{SGM}) as an inverse surrogate for regional brain atrophy are depicted in Figure 12. Data suggested a disease-dependent reduction of 10% in NV_{SGM} ($t = -5.63$, $p < 0.001$). No difference in NV_{WM} was observed between cohorts ($t = 0.95$, $p = 0.34$).

NV_{SGM} and φ_{SGM} were significantly correlated (MS: $r = +0.30$, $p = 0.01$; HC: $r = +0.29$, $p = 0.05$) (Figure 13, Table 7). However, there was no association between NV_{WM} and WM viscoelasticity.

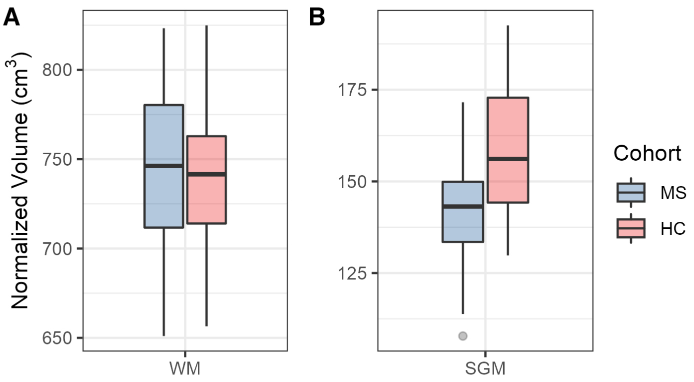

Figure 12: Distribution of normalized WM/SGM volumes. Descriptive statistics (Mean ± SD in cm^3): NV_{WM}: MS 746 ± 43, HC 738 ± 39; NV_{SGM}: MS 142 ± 13, HC 158 ± 17.

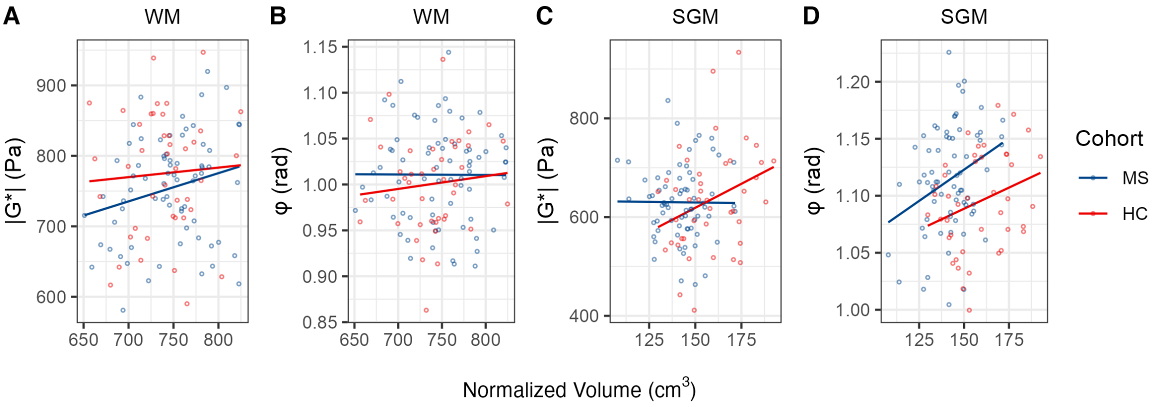

Figure 13: G^* as a function of normalized WM/SGM volumes

G^*	Cohort	NV_{WM}	NV_{SGM}
$\lvert G^*\rvert$	MS	$r = +0.23$, $p = 0.06$	$r = +0.01$, $p = 0.94$
	HC	$r = +0.06$, $p = 0.71$	$r = +0.31$, $p = \mathbf{0.05}$
φ	MS	$r = -0.01$, $p = 0.97$	$r = +0.30$, $p = \mathbf{0.01}$
	HC	$r = +0.10$, $p = 0.52$	$r = +0.29$, $p = \mathbf{0.05}$

Table 7: Pearson's correlations between normalized WM/SGM volumes and G^*

Relating atrophy to age, data showed a significant correlation between age and NV_{WM} in patients (MS: $\rho = -0.48$, $p < 0.001$; HC: $\rho = +0.09$, $p = 0.58$) but not between age and NV_{SGM} (MS: $\rho = -0.13$, $p = 0.30$; HC: $\rho = -0.28$, $p = 0.08$). (Figure 14).

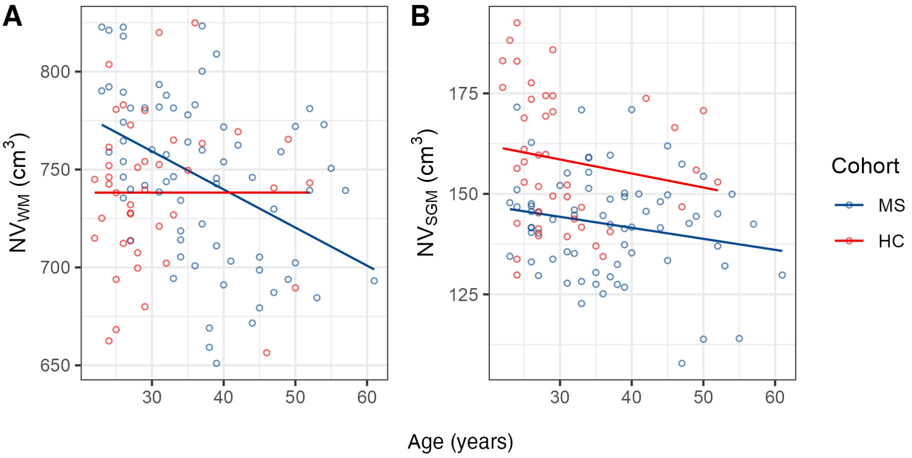

Figure 14: Normalized WM/SGM volumes as functions of age

4.3 Patient-specific Analyses

4.3.1 Expanded Disability Status Scale

EDSS distribution deviated significantly from normality ($p < 0.001$). φ_{SGM} was significantly negatively correlated with EDSS ($\rho = -0.27$, $p = 0.02$) (Figure 15, Table 8). There was no association between $|G^*|$ and EDSS. Furthermore, there were no significant differences in all viscoelasticity measures between EDSS subgroups low (≤1.5) and high (>1.5) (Figure 16, Table 9).

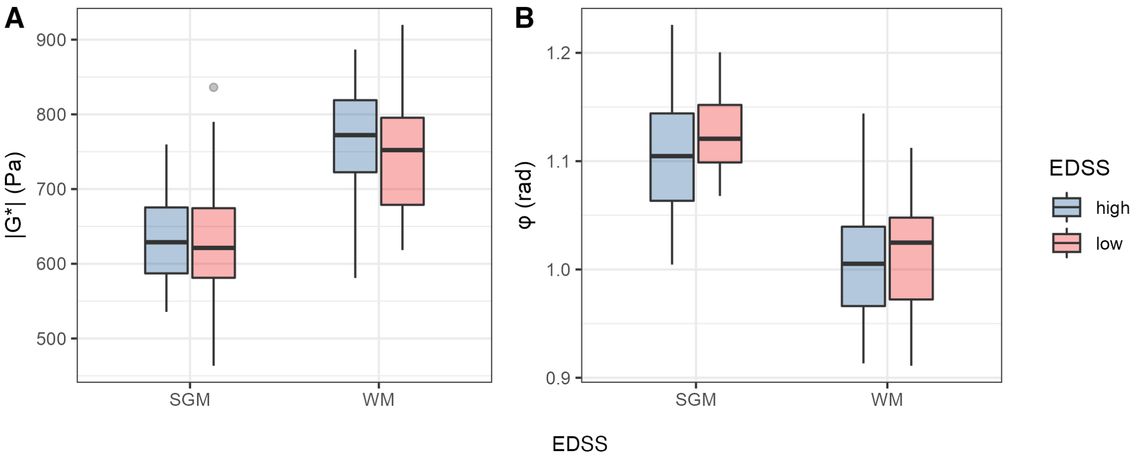

Figure 15: G^* as a function of EDSS. Jitter was added to avoid overlapping data points.

G^*	WM	SGM
$\|G^*\|$	$\rho = +0.04$, $p = 0.76$	$\rho = -0.03$, $p = 0.83$
φ	$\rho = -0.21$, $p = 0.08$	$\rho = -0.27$, $p =$ **0.02**

Table 8: Spearman's rank correlations between EDSS and G^*

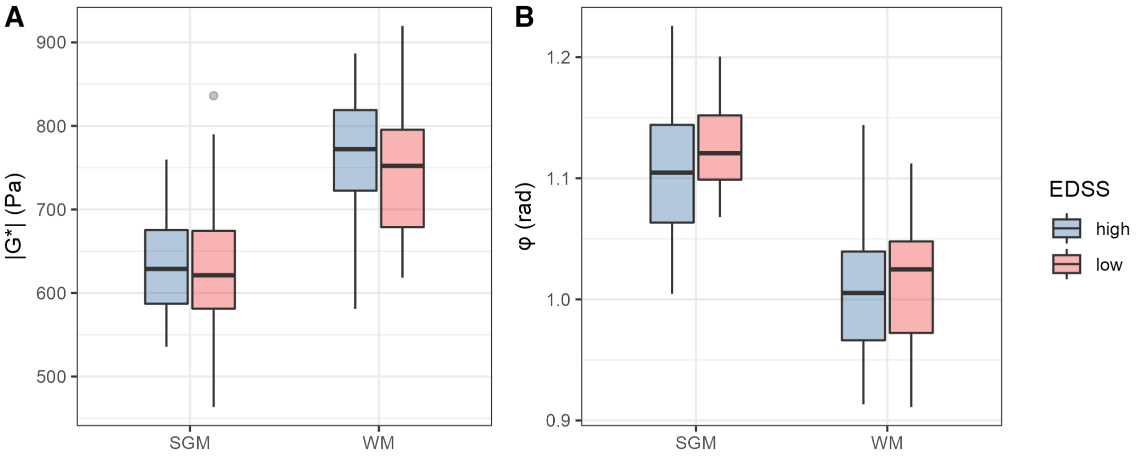

Figure 16: Distribution of G^* according to EDSS subgroups. EDSS subgroups low (≤1.5) and high (>1.5) were formed with respect to median EDSS.

	WM				SGM			
G^*	Mean±SD EDSS low	Mean±SD EDSS high	Δ	Student's t	Mean±SD EDSS low	Mean±SD EDSS high	Δ	Student's t
$\lvert G^*\rvert$	749 ± 79	760 ± 71	1%	$t = +0.59$, $p = 0.55$	630 ± 85	630 ± 60	0%	$t = +0.04$, $p = 0.97$
φ	1.02 ± 0.05	1.00 ± 0.05	2%	$t = -1.06$, $p = 0.29$	1.12 ± 0.03	1.10 ± 0.06	2%	$t = -1.92$, $p = 0.06$

Table 9: Differences in G^* in EDSS subgroups. Units $|G^*|$ in Pa, φ in rad. Δ depicts percental differences between means.

4.3.2 Phenotype

Data for G^* are reported descriptively for phenotype subgroups SPMS ($n = 4$) and CIS/RRMS ($n = 64$) (Table 10). There was a reduction of median $|G^*|$ and φ in SPMS relative to CIS/RRMS patients.

	WM			SGM		
G^*	Median (IQR) SPMS	Median (IQR) CIS/RRMS	Δ Median	Median (IQR) SPMS	Median (IQR) CIS/RRMS	Δ Median
$\lvert G^*\rvert$ (Pa)	720 (46)	767 (107)	−47	586 (10)	627 (85)	−41
φ (rad)	0.98 (0.04)	1.02 (0.08)	−0.04	1.04 (0.03)	1.11 (0.06)	−0.07

Table 10: Statistics of G^* according to MS phenotype

4.3.3 Disease Duration

Duration of disease distribution deviated significantly from a normal distribution ($p < 0.001$). There was a significant negative correlation between $|G^*|$ and disease duration (WM: $\rho = -0.29$, $p = 0.01$; SGM: $\rho = -0.23$, $p = 0.05$) (Figure 17, Table 11). No correlation was found between disease duration and φ.

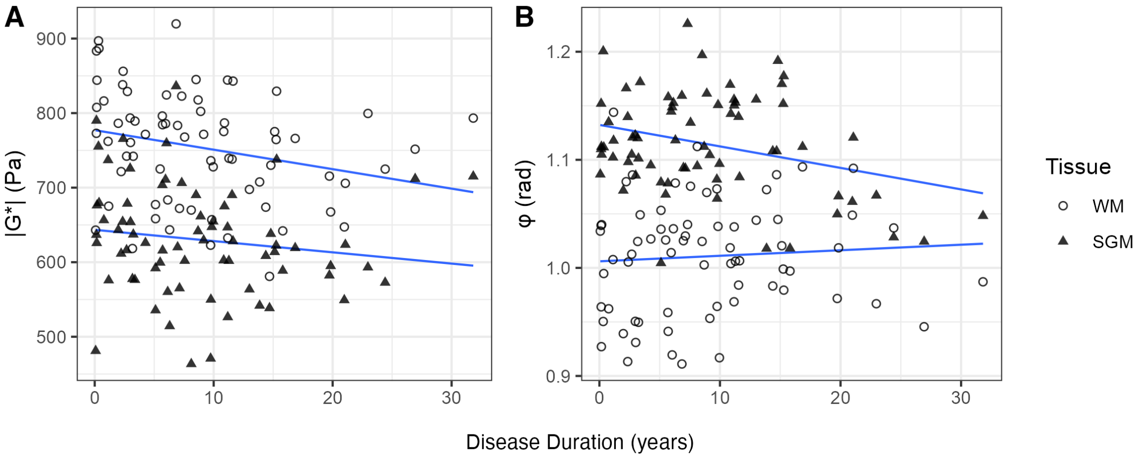

Figure 17: G^* as a function of duration of disease

G^*	WM	SGM
$\lvert G^*\rvert$	$\rho = -0.29$, $p =$ **0.01**	$\rho = -0.23$, $p =$ **0.05**
φ	$\rho = +0.11$, $p = 0.36$	$\rho = -0.15$, $p = 0.22$

Table 11: Spearman's rank correlations between disease duration and G^*

4.3.4 Lesion Load

Lesion load distribution deviated significantly from normality ($p < 0.001$). Neither $|G^*|$ nor φ were associated with lesion load (Figure 18, Table 12).

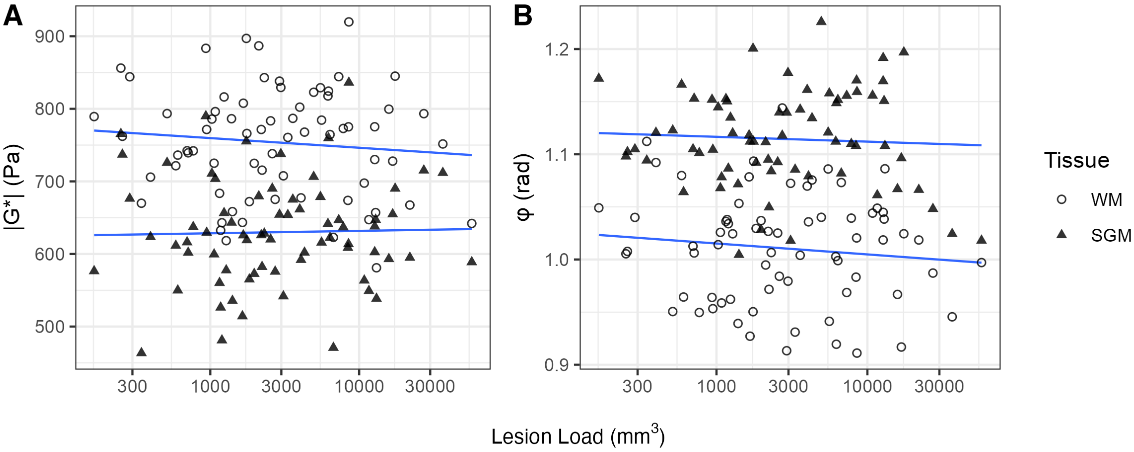

Figure 18: G^* as a function of lesion load. Note the logarithmic x-axis.

G^*	WM	SGM
$\lvert G^*\rvert$	$\rho = -0.05$, $p = 0.68$	$\rho = +0.03$, $p = 0.82$
φ	$\rho = -0.06$, $p = 0.58$	$\rho = +0.008$, $p = 0.95$

Table 12: Spearman's rank correlations between lesion load and G^*

4.3.5 Multiple Linear Regression

As shown above, φ_{SGM} correlated significantly with age, EDSS and NV_{SGM}. Whereas association between age and EDSS was significant ($\rho = 0.33$, $p = 0.005$), there was neither a significant correlation between age and NV_{SGM} ($\rho = -0.13$, $p = 0.30$) nor between EDSS and NV_{SGM} ($\rho = -0.18$, $p = 0.13$).

Multiple linear regression was performed according to the model $\varphi_{SGM} = \beta_0 + \beta_1 \cdot age + \beta_2 \cdot NV_{SGM}$. The model suggested both age and NV_{SGM} as significant explanatory variables ($F_{2,67} = 8.63$, $R^2 = 0.18$, $p < 0.001$; age: $t = -3.08$, $p = 0.003$; NV_{SGM}: $t = 2.13$, $p = 0.04$).

According to the model $\varphi_{SGM} = \beta_0 + \beta_1 \cdot age + \beta_2 \cdot EDSS$, age was the only significant explanatory variable ($F_{2,67} = 8.95$, $R^2 = 0.17$, $p < 0.001$; age: $t = -2.55$, $p = 0.01$; EDSS: $t = -1.88$, $p = 0.06$).

4.3.6 Lesions and Normal-Appearing White Matter

After filtering for lesion size and CSF distance as shown in subsection 3.5.2, lesion data was reduced to 63 patients. Patient-wise connecting lines in Figure 19 indicated no difference in $|G^*|$ between lesions (L1) and their surrounding NAWM (N1) and a more weakly diffuse relation between non-symmetrical lesions (L2) and their corresponding contralateral NAWM (N2). φ seemed to be marginally but consistently lower in lesions compared to surrounding NAWM.

No normality could be assumed in lesion ROIs (e.g., $p = 0.02$ for L1 in $|G^*|$). Paired Wilcoxon signed-rank tests indicated no significant within-cohort differences in $|G^*|$ between L1/N1 and L2/N2. There was no significant between-cohort difference for G^* between lesions and their corresponding averaged WM in HCs. However, there was a significant difference in φ between L2/N2 ($V = 561$, $p = 0.002$) (Table 13).

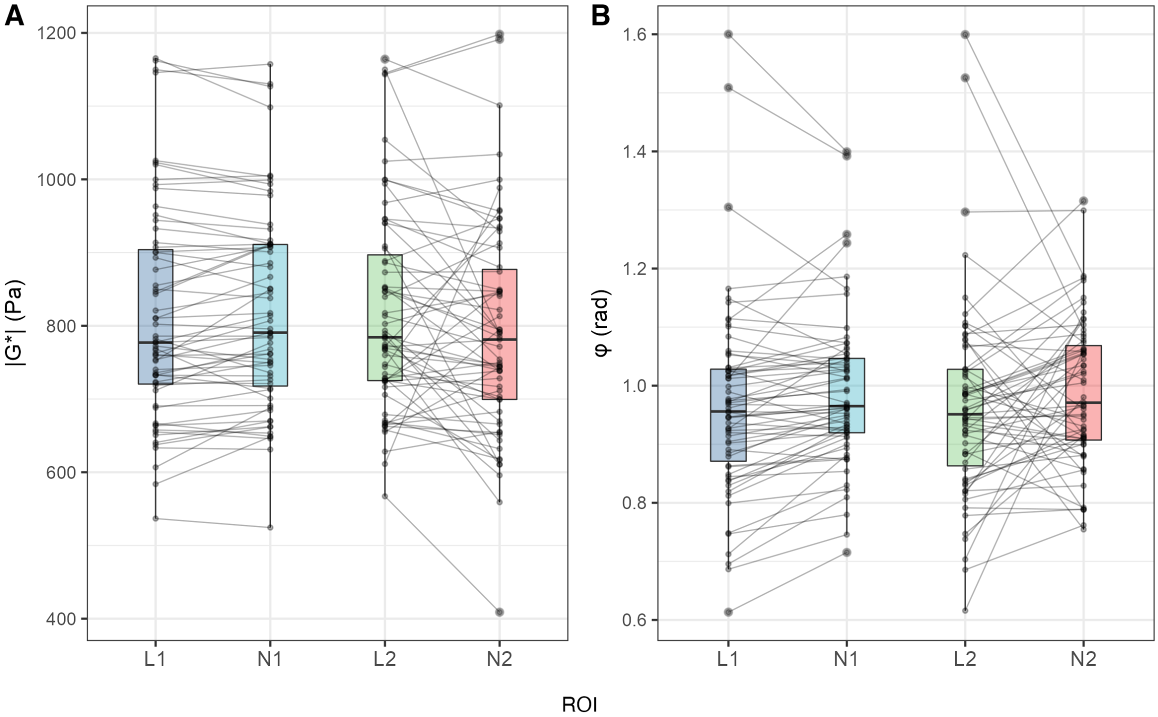

Figure 19: Distribution of G^* in lesions and corresponding NAWM. In each patient, mean $|G^*|$ (A) and φ (B) were calculated for following ROIs: all lesions (L1), lesion-surrounding NAWM (N1), strictly unilaterally occuring (i.e., non-symmetric) lesions after transformation to MNI152 space (L2) and their corresponding contralateral NAWM in MNI152 space (N2). Distributions are represented as boxplots with added individual data points and patient-wise connecting lines.

	$\lvert G^* \rvert$ (Pa)		φ (rad)	
ROI (figure label)	Median (IQR)	Wilcoxon signed-rank	Median (IQR)	Wilcoxon signed-rank
All lesions (L1)	777 (184)		0.96 (0.16)	
Surrounding NAWM (N1)	791 (193)	$V = 853$, $p = 0.29$	0.97 (0.13)	$V = 561$, $p =$ **0.002**
Averaged WM in HC	805 (75)	$V = 1891$, $p = 0.65$	0.96 (0.06)	$V = 1932$, $p = 0.80$
Non-symmetric lesions (L2)	784 (172)		0.95 (0.16)	
Contralat. NAWM (N2)	781 (178)	$V = 1302$, $p = 0.05$	0.97 (0.16)	$V = 752$, $p = 0.08$

Table 13: Statistics of G^* in lesions and corresponding NAWM

Pairwise differences ΔX of data points as connected above are depicted in Figure 20. Dominated by positive values for ΔX, histograms for $\Delta\varphi$ (C, D) indicated φ to be lower in lesions relative to surrounding NAWM.

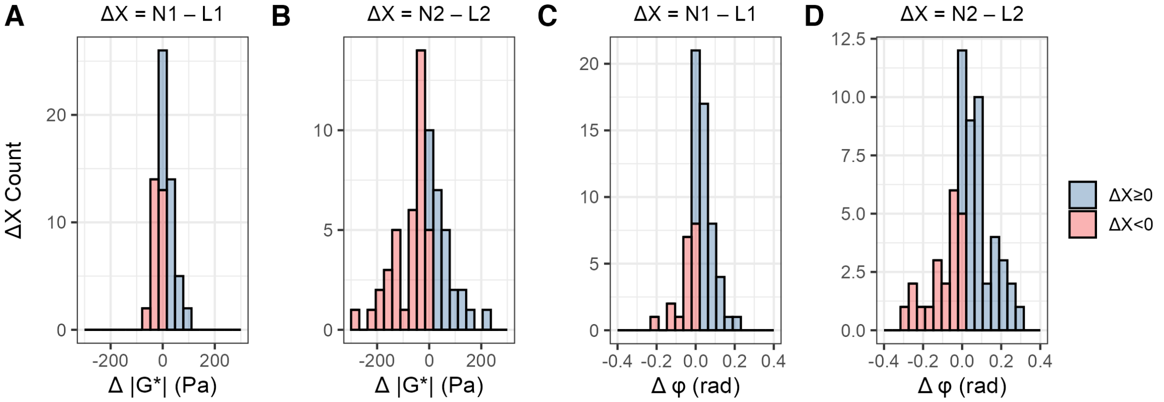

Figure 20: Within-patient differences in G^* between lesions and NAWM. Each histogram is presenting count of pairwise differences ΔX of $\lvert G^* \rvert$ (A, B) and φ (C, D) in ROIs as labelled above. Positive ΔX (blue) indicate a reduced mean stiffness in lesions (ROIs L1/L2) relative to NAWM (ROIs N1/N2) within a patient. Equal x-axis limits for A/B and C/D. Descriptive statistics (Median (IQR)): ΔX_A: 4 (40); ΔX_B: -22 (93); ΔX_C: 0.02 (0.07); ΔX_D: 0.02 (0.14).

4.4 Inter-Cohort Analyses

According to Table 4, normality of G^* was assumed in WM and SGM. However, in the HC cohort, distribution of φ significantly deviated from normality in the thalamus ($p = 0.002$) and occipital lobe ($p = 0.02$), which is why Wilcoxon rank-sum tests were conducted to test for inter-cohort differences in G^* in subregions.

4.4.1 White and Subcortical Grey Matter

In both cohorts, $\lvert G^* \rvert$ was significantly higher in WM compared to SGM (MS: +20%, HC: +18%; $p < 0.001$ each). Furthermore, φ was significantly lower in WM relative to SGM (MS: -10%, HC: -8%; $p < 0.001$ each).

Data suggested no significant differences in $\lvert G^* \rvert_{WM,\ SGM}$ and φ_{WM} between cohorts (Figure 21, Table 14). A weak trend towards an increase in φ_{SGM} (2%) was observed in patients ($t = 2.28$, $p = 0.03$). There was no difference in G^* between NAWM in patients and WM in HCs.

Multiple linear regression was conducted for the response variable φ in SGM according to $\varphi_{SGM} = \beta_0 + \beta_1 \cdot cohort + \beta_2 \cdot age + \beta_3 \cdot NV_{SGM}$. The model indicated that all explanatory variables significantly predict φ_{SGM} ($F_{3,108} = 9.76$, $R^2 = 0.21$, $p < 0.001$; cohort: $t = -4.41$, $p < 0.001$; age: $t = -3.46$, $p < 0.001$; NV_{SGM}: $t = 2.68$, $p = 0.009$).

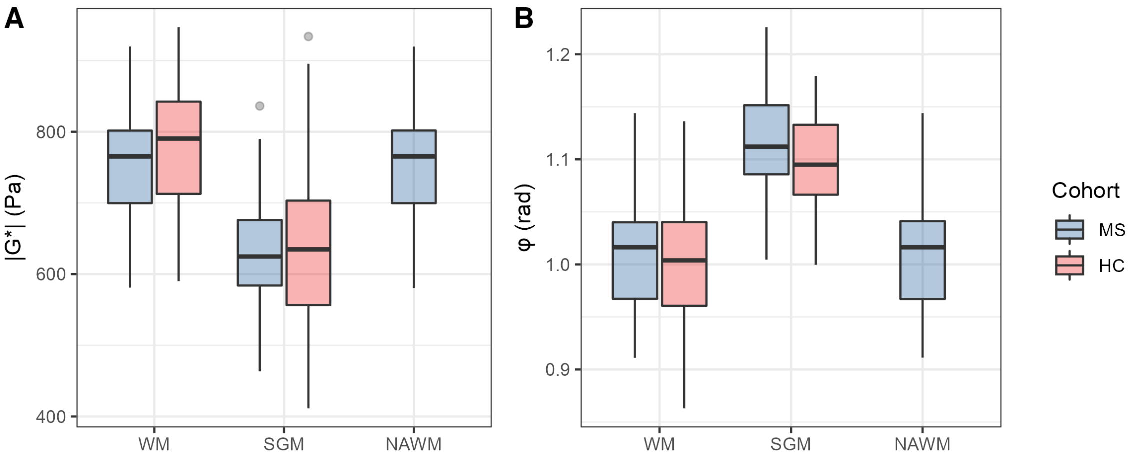

Figure 21: Distribution of G^* in WM, SGM and NAWM

	$\lvert G^*\rvert$ (Pa)				φ (rad)			
ROI	Mean±SD MS	Mean±SD HC	Δ	Student's t	Mean±SD MS	Mean±SD HC	Δ	Student's t
WM	754 ± 75	775 ± 88	3%	$t = -1.30$, $p = 0.20$	1.01 ± 0.05	1.00 ± 0.05	1%	$t = 0.99$, $p = 0.32$
NAWM	754 ± 75	–	3%	$t = -1.31$, $p = 0.20$	1.01 ± 0.05	–	1%	$t = 1.04$, $p = 0.30$
SGM	630 ± 74	635 ± 106	<1%	$t = -0.28$, $p = 0.78$	1.11 ± 0.05	1.09 ± 0.04	2%	$t = 2.28$, $p = \mathbf{0.03}$

Table 14: Inter-cohort differences in G^* in WM, SGM and NAWM. NAWM was related to WM in HCs. Δ relates to percental differences between means.

4.4.2 Subregions

As illustrated in Figure 22, data indicated cohort-independent differences in G^* between subregions within WM and SGM, respectively. Notably, there was a prominent increase in $|G^*|$ in the putamen (33%) as well as frontal and parietal lobes (17%), whereas for φ, higher values were observed in the insular and temporal lobes (12%) (data reported with respect to residual ROIs; $p < 0.001$ each) (Table 15).

In patients, there was a significant increase in φ in occipital WM ($p = 0.02$) and thalamic SGM ($p = 0.002$) relative to HCs.

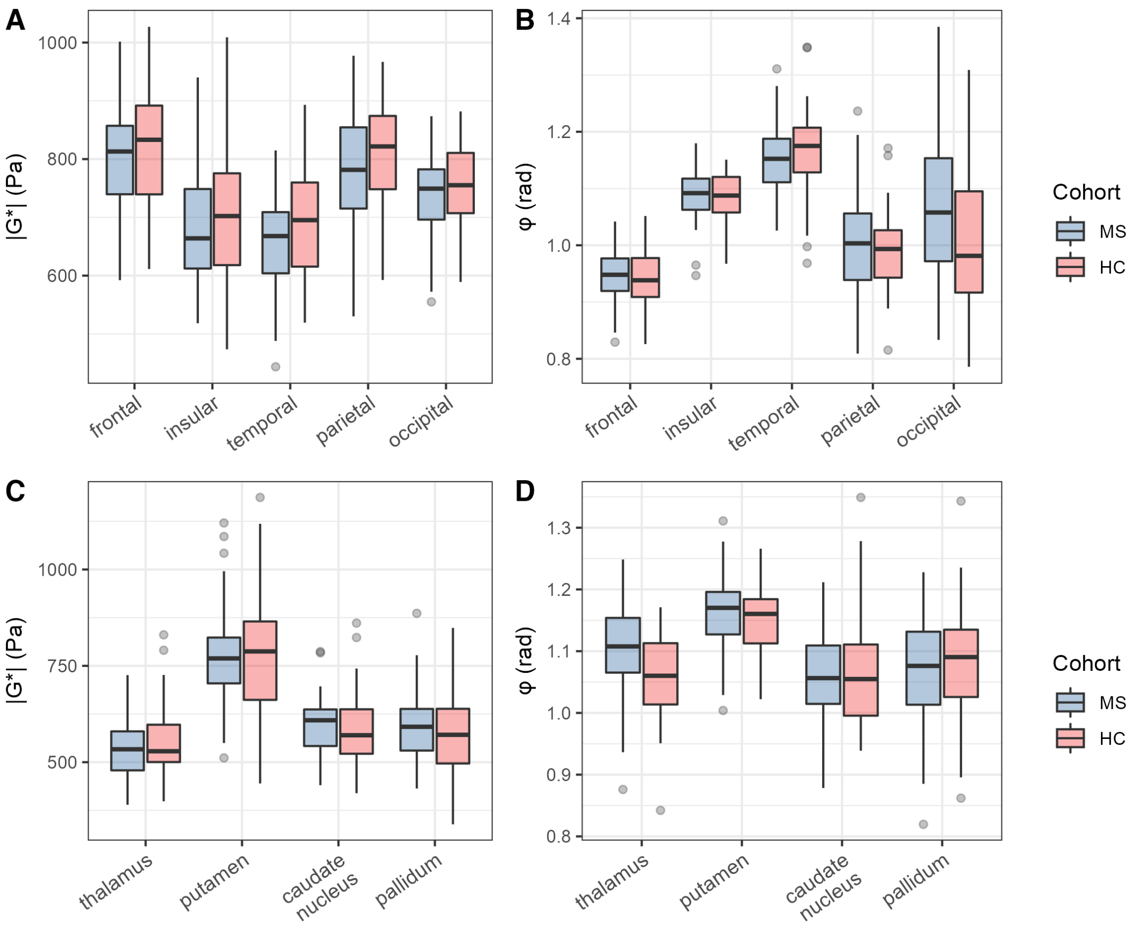

Figure 22: Distribution of G^* in WM/SGM subregions

	$\lvert G^*\rvert$ (Pa)			φ (rad)		
ROI	Median (IQR) MS	Median (IQR) HC	Wilcoxon rank-sum	Median (IQR) MS	Median (IQR) HC	Wilcoxon rank-sum
WM subregions						
frontal	813 (117)	833 (152)	$V = 1317$, $p = 0.36$	0.95 (0.06)	0.94 (0.07)	$V = 1602$, $p = 0.43$
insular	664 (136)	702 (158)	$V = 1294$, $p = 0.29$	1.09 (0.05)	1.08 (0.04)	$V = 1506$, $p = 0.83$
temporal	668 (105)	695 (144)	$V = 1176$, $p = 0.08$	1.15 (0.08)	1.18 (0.08)	$V = 1263$, $p = 0.21$
parietal	782 (139)	822 (126)	$V = 1201$, $p = 0.11$	1.00 (0.12)	0.99 (0.08)	$V = 1563$, $p = 0.58$
occipital	749 (86)	755 (103)	$V = 1376$, $p = 0.57$	1.06 (0.18)	0.98 (0.18)	$V = 1852$, $p =$ **0.02**
SGM subregions						
thalamus	533 (101)	528 (97)	$V = 1342$, $p = 0.44$	1.11 (0.09)	1.06 (0.10)	$V = 1988$, $p =$ **0.002**
caudate	609 (95)	570 (115)	$V = 1686$, $p = 0.20$	1.06 (0.09)	1.05 (0.12)	$V = 1485$, $p = 0.93$
putamen	769 (119)	787 (203)	$V = 1418$, $p = 0.76$	1.17 (0.07)	1.16 (0.07)	$V = 1672$, $p = 0.23$
pallidum	592 (108)	571 (142)	$V = 1571$, $p = 0.55$	1.08 (0.12)	1.09 (0.11)	$V = 1342$, $p = 0.44$

Table 15: Inter-cohort differences in G^* in WM/SGM subregions

5 Discussion

In any medical field, scientists and physicians strive for acquiring a comprehensive picture of disease in patients. This endeavor is still unsatisfying in MS, limiting prediction of clinical course and evaluation of treatment efficacy.

This thesis sought to evaluate MRE as a paraclinical tool in diagnosis and assessment of MS and to expand knowledge about pathophysiological processes driving disease progression. While prior research focused on global alterations in viscoelasticity in the MS brain, this work aimed at gaining insight into localized processes. Using a novel low-frequency DENSE sequence, achievement of better tissue penetration and reduction of imaging artifacts compared to previous work was expected.

5.1 Recapitulation

In a controlled experiment, 73 MS patients and 42 healthy controls were examined. A subject's head was mechanically excited at a frequency of 20 Hz. By means of a motion-sensitive MRI sequence [36, 85], tissue displacement was captured, from which a spatial map of the complex shear modulus G^* was reconstructed.

G^* can be split into two independent parts: whereas $|G^*|$ is a measure for how much tissue resists deformation and can be understood as an equivalent to palpatory stiffness, φ describes the ratio of viscosity to elasticity in tissue [71].

Subject-wise spatial means of G^* were calculated for global and subregional WM and SGM. SGM was defined as the sum of all subcortical GM regions investigated: thalamus, caudate, pallidum and putamen. WM was further parcellated into frontal, insular, temporal, parietal and occipital lobes. Viscoelasticity data were compared between cohorts and were related to demographic, clinical and radiological characteristics. In the patient cohort, special emphasis has been put on the mechanical characterization of T2w lesions and NAWM.

5.2 Baseline Brain Viscoelasticity

In the following, viscoelasticity findings concerning variables not related to disease are put into context and discussed.

5.2.1 Comparability to Existing Literature

As an evolving modality, in MRE, crucial aspects in the experimental setup and post-processing pipeline are still lacking standardization. That is why challenges and pitfalls, that may occur when comparing results to prior research, need to be identified.

Most authors present viscoelasticity data in the form of $|G^*|$ and φ, which is in conformity with this study's methodology. However, other studies report different parameters, necessitating mathematical reformulation for data comparison. Another aspect is that reconstructed viscoelasticity measures are inherently frequency-dependent and therefore cannot be generalized per se. Transformation into a generalized form, however, requires fitting to a rheological model, which further depends on a set of assumptions and is only feasible in multi-frequency experiments.

Since the main objective of this study was to relate stiffness parameters between groups within one setup, a single-frequency approach was chosen and no rheological fitting was done.

In multi-frequency MRE studies by Sack et al. [41], Streitberger et al. [51], and Wuerfel et al. [54], estimates of G^* were fitted to a springpot model. This way, two frequency-independent constants were derived, namely the elasticity modulus μ and the interpolation factor α. Albeit mathematically incorrect, relative changes in μ and α can roughly be translated to $|G^*|$ and φ, respectively.

In an MRE standard-space atlas comprising averaged data of 134 volunteers, Hiscox et al. [101] presented viscoelasticity parameters as the combined quantities shear stiffness $\mu = 2 \cdot |G^*| \cdot \frac{2}{G' + |G^*|}$ and damping ratio $\xi = \frac{G''}{G'}$, a presentation also used by McIlvain et al. [63], Murphy et al. [98], and Johnson et al. [102]. For data comparison, these measures were reformulated to $|G^*|$ and φ.

Overall, reliable data on brain viscoelasticity is sparse, partially contradictory and measured values can vary by orders of magnitude [41, 46, 60, 101], which is why it is crucial to account for methodology. Inconsistency can be partially explained by the brain's sensitivity to actuation frequency and strain stiffening [103]. Care has to be taken when comparing MRE data to other elastography modalities such as indentation experiments, which can yield contradictory results when applied to cellular or macroscopic scales [104, 105]. Tissue stiffness is as well sensitive to perfusion pressure [106], which has to be considered in *ex vivo* studies.

5.2.2 White and Grey Matter

Early as well as recent MRE studies disagree on the relative stiffness of WM and GM. Unfortunately, this also accounts for other modalities such as indentation testing [31, 104, 105, 107, 108], which is why to date, brain MRE hypotheses can hardly be verified or falsified.

Studies indicating a reduction in GM viscoelasticity with respect to WM report a decrease between 20% and 50% in $|G^*|$, while φ remains more or less constant [60–62]. However, opposing data exist [28, 46, 98, 101, 109]. Particularly for SGM, some studies report higher stiffness compared to WM [102, 110, 111].

In this work, a group-independent increase in $|G^*|$ (20%) and decrease in φ (9%) in WM relative to SGM was observed, suggesting higher stiffness in WM ($p < 0.001$). With a mean stiffness $|G^*|$ of 762 ± 81 Pa (WM) and 632 ± 87 Pa (SGM) across all participants, the values measured in this study rank within the lower spectrum of existing brain stiffness data. In agreement with previous work, data showed a relative standard deviation of ~10% across subjects in all global measurements.

This study's observations are consistent with data of other modalities, e.g., indentation experiments on tissue scale in bovine and porcine brains conducted by Weickenmeier et al. [58] and van Dommelen et al. [31]. Data are further bolstered by histological considerations with WM structurally supported by organized fibre bundles, thus showing a higher degree of adherence than GM [107]. In contrast, the observed difference in φ between white and grey matter has not been documented in previous brain MRE experiments so far.

As discussed later, deduction of physiological correlates from viscoelasticity parameters is challenging at best. In addition, account must be taken of the presence of imaging artifacts. For instance, the observed behavior of φ could be explained by the sensitivity of φ to wave scattering, which is particularly pronounced in proximity to tissue boundaries such as CSF/GM [62].

5.2.3 Subregions

In accordance with an atlas presented by Hiscox et al. [101] ($N = 134$), data indicated a group-independent significant increase in $|G^*|$ of 20% in frontal, parietal and occipital lobes compared to insular or temporal lobes (mean $|G^*|$ frontal: 808 ± 94 Pa vs. temporal: 669 ± 90 Pa; $p < 0.001$). However, other authors report opposing data, e.g., McIlvain et al. [63] measured higher μ in the parietal and temporal lobes in both adolescents and adults.

Among all intracerebral regions in the atlas provided by Hiscox et al., the putamen showed highest stiffness μ, which matches well this study's SGM data (mean $|G^*|$ putamen: 778 ± 134 Pa vs. residual SGM: 578 ± 101 Pa; $p < 0.001$). However, measurements could be confounded by noise from fibre tracts in the internal and external capsule surrounding the putamen.

5.2.4 Sex and Age

In a multi-frequency MRE study by Sack et al. [41] investigating sex and age-related effects in brain viscoelasticity in three transverse slices at ventricle level, an annual decline in μ of 0.8% was observed ($N = 55$). A later study by Sack et al. [64] was in accordance with their previous findings ($N = 66$). Similarly, in an MRE study analyzing subregional differences in viscoelasticity, Arani et al. [65] reported a regional-dependent decline in cerebral stiffness of approximately 11 ± 2 Pa per year (0.4%) ($N = 45$).

In accordance with the literature, the present data suggested a non-significant age-dependent decline in $|G^*|$ in WM and SGM in both cohorts. Furthermore, a negative correlation between age and φ_{SGM} was observed, which has not been described to date.

Whereas Sack et al. suggested sexual dimorphism with cerebral viscoelasticity in females to be 9% stiffer, this was not confirmed in the authors' later findings [41, 64]. Arani et al. stated that only the temporal and occipital lobes show sexual dimorphism with an increase of approximately 230 Pa (8%) in females. In agreement with Sack et al. [41], this study found sex as a weak predictor for brain stiffness with a reduction of $|G^*|$ and φ in males compared to females.

Albeit below significance level, visual data inspection suggested equally strong effects of aging on φ_{SGM} in HCs. Lack of significance in the control cohort could be attributed to poor age distribution and smaller sample size, as discussed later.

5.3 Brain Viscoelasticity in Multiple Sclerosis

5.3.1 Prior Studies

In a first MRE study comparing MS patients to a matched HC group conducted by Wuerfel et al. [54] ($N_{MS} = 45$, $N_{HC} = 34$), in patients, a reduction in springpot constant μ of 13% at a constant interpolation factor α was observed. In contrast, stiffness parameters were neither correlated to EDSS, lesion load nor brain parenchymal fraction (BPF), which is an estimate for brain atrophy. The MS cohort comprised of RRMS phenotype patients with a mean EDSS of 1.6 (range $0 - 4$), matching well this study's patient cohort characteristics (median EDSS 1.5, range $0 - 5.5$).

Investigating progressive phenotype patients using MRE, Streitberger et al. [51] reported a significant decrease in both springpot constants μ (20%) and α (6%) in comparison to a matched HC group ($N_{PPMS} = 6$, $N_{SPMS} = 17$, $N_{HC} = 38$). In agreement with Wuerfel et al., neither μ nor α correlated to EDSS, BPF or disease duration. Both authors shared identical methodology: data were acquired from three slices on corpus callosum level through a multi-frequency setup ($f = 25 - 62.5$ Hz) at identical acquisition parameters. Data were averaged across slice parenchyma without differentiating between WM and GM. Reported $|G^*|$ for individual frequencies indicated a greater between-cohort difference for lower actuation frequencies, suggesting low frequencies to be eligible for revealing diffuse pathology in the MS brain.

Investigating CIS patients, relative to an age-matched HC group, Fehlner et al. [57] observed a 14% decrease in $|G^*|_{WM}$ at a constant φ ($N_{CIS} = 16$; $N_{HC} = 33$). Whole-brain parenchyma decrease was 10%. Interestingly, MRE showed no difference in patients who later developed MS.

In an MRE study on the corpus callosum of mice after cuprizone-induced demyelination, Schregel et al. [52] observed φ to linearly correlate with myelin content, whereas $|G^*|$ was assumed to reflect ECM integrity (N not reported).

5.3.2 Inter-Cohort Analyses

According to the research done for this thesis, this is the first work that separately explored WM, SGM and subregional viscoelasticity in the MS brain by means of MRE. Existing studies restricted image acquisition to selected slices or conducted analysis without parenchymal differentiation [51, 54] or solely on global WM [57].

In contrast to data reported by the authors mentioned above, no relevant alteration in global WM and SGM viscoelasticity was observed between cohorts. Group-averaged data showed a minor trend towards a decrease in $|G^*|$ and an increase in φ in patients in both WM and SGM, ranging between 1% and 3%. However, increase in φ_{SGM} was significant ($p = 0.03$). Differences in $|G^*|$ could be entirely explained by a between-cohort mismatch in age, which was significantly higher in patients. On the other hand, since φ_{SGM} is inversely correlated with age, a significant rise in φ_{SGM} in patients is remarkable.

By subregion analysis, in φ, a significant increase was observed in the thalamus in patients ($p = 0.002$). As known from the literature, the thalamus is among the first deep grey structures undergoing neurodegeneration and atrophy in MS [112] or CIS [113]. Due to its connective role to cortical and subcortical areas, it is assumed that axonal transection in WM promptly impacts the thalamus integrity [114, 115].

5.3.3 Clinical and Radiological Characteristics

5.3.3.1 Disability, Lesion Load, Disease Duration

In accordance with Wuerfel et al. and Streitberger et al., in this study, neither T2w lesion load nor EDSS were significantly correlated with $|G^*|$ or φ. This finding stresses that diffuse degenerative processes dominate viscoelasticity changes in the MS brain. In turn, it substantiates that lesion load is not a sensitive measure for progression of disease.

Contrary to data by Streitberger et al., disease duration was observed to inversely correlate with $|G^*|_{WM}$ ($p = 0.01$), whereas φ_{WM} was unaffected. This is remarkable, since neither atrophy nor EDSS were associated with $|G^*|_{WM}$ nor was there a pronounced effect of age on $|G^*|_{WM}$.

5.3.3.2 Atrophy

In MS, brain atrophy is used as a quantitative radiological measure for progression of disease [23, 24, 116]. However, atrophy estimates depend on post-processing methods and are confounded by age or pseudoatrophy, among others [23, 117, 118]. In addition, the pathophysiology behind atrophy is not fully understood to date [119].

The effect of brain volume and atrophy on viscoelasticity was investigated by Sack et al. in healthy volunteers ($N = 66$) [64]. In their study, atrophy was negatively correlated with μ and α but was not an independent predictor in a multiple regression analysis. Similarly, no correlation was found by Wuerfel et al. and Streitberger et al. in MS patients.

While previous research did not relate viscoelasticity to WM and GM atrophy separately, in line with the findings mentioned above, this work found that WM atrophy is neither reflected by $|G^*|_{WM}$ nor φ_{WM}. However, NV_{SGM} was observed to significantly correlate with φ_{SGM}.

Interestingly, while SGM atrophy was significantly higher in patients, it was not correlated to age ($p = 0.30$). By multiple regression analysis, it was further shown that age and SGM atrophy are independent predictors for a decrease in φ_{SGM}, suggesting two independent processes. This is in accordance with Sack et al., who reported that the annual decline in stiffness is only partially explained by atrophy, surpassing it by a factor of three.

It stands to reason that aging and disease contribute to a degradation of the brain's microstructure, which is reflected in both atrophy and changes in viscoelasticity. However, both aging and atrophy suggested comparable correlation coefficients for φ_{SGM}. This is why it can be assumed that viscoelasticity parameters are not suitable for differentiating between disease-related atrophy and aging as a confounding factor.

5.3.3.3 Lesions and Normal-Appearing White Matter

A novelty in this work is the mechanical characterization of T2w lesions relative to NAWM. Autopsy is capable of differentiating between various plaque types, reflecting the allegedly hidden heterogenity of lesions in conventional MRI [120, 121]. Since correlation between T2w lesion load and clinical picture is poor [16], *in vivo* lesion characterization is subject of active research [122].

According to Urbanski et al. [123], *ex vivo* indentation testing in the demyelination-induced mouse and post-mortem human MS brain indicated that acutely demyelinated lesions were reduced in stiffness. In contrast, chronic demyelination led to increased stiffness, which was associated with a characteristic ECM deposition. However, indentation analyses by Weickenmeier et al. [58] suggested proportionality between local viscoelasticity and myelin content, hypothesizing myelin itself as a major contributor to stiffness.

WM physiologically exhibits regional variations in viscoelasticity [98, 101], which is why in a within-patient approach, this thesis referenced global lesion stiffness to corresponding parts in contralateral NAWM. In many patients, however, symmetrical lesion distribution substantially reduced data quantity due to lack of contralateral reference tissue. In a second approach, lesion stiffness was therefore related to NAWM in the close vicinity of lesions. In order to account for MRE's low spatial resolution, lesions below a volume of $50\,\mathrm{mm}^3$ were excluded, which was considered a middle ground between data quantity and quality.

The present data indicated a marginal but significant reduction in φ of 1% in lesions relative to surrounding NAWM ($p = 0.002$). It cannot be ruled out that this observation originated from methodology: comparison to surrounding tissue inevitably expands measurements closer to CSF, where φ is presumably subjected to low φ noise.

A weakness in this study's methodology is the comparison of global masks, although lesions can exhibit opposite alterations in viscoelasticity [123]. However, by not applying contrast agents, no identification of active lesions was possible. Pathophysiological considerations would propose that acute inflammation reduces viscoelasticity through edema. This was in fact observed in a study on mice with experimental autoimmune encephalitis, in which acute inflammation in the absence of demyelination corresponded to a reversible decrease in $|G^*|$ [53].

In future studies, pairing MRE with contrast-enhanced T1w imaging and SWI could help relating inactive, active, chronic active and chronic inactive lesions to mechanical alterations [124].

5.3.4 Pathophysiological Interpretation

In the literature, brain viscoelasticity was related to a number of physiological parameters (myelin content, neuronal and axonal density, ECM composition, perfusion pressure) and diffuse pathological processes (inflammation, glial scarring, neurodegeneration and demyelination), to name a few [52, 53, 58, 59, 125].

In this study, although between-cohort analyses revealed no substantial global alteration in brain viscoelasticity in MS, correlation to clinical features and radiological findings suggested viscoelasticity parameters to indirectly reflect combined aspects of disease. Contrary to prior research, these alterations were predominantly found in φ_{SGM} with age and atrophy independently correlating with a decline in φ_{SGM}. Conversely, φ_{SGM} in MS was significantly higher than in HCs, predominantly in the thalamus. Disease duration was the only variable associated with a decline in $|G^*|$.

The MRE study conducted by Schregel et al. on cuprizone-fed mice aimed at differentiating between viscoelastic correlates of demyelination, axonal degeneration and ECM deposition by means of histological analyses. In healthy mice, during adolescence – when completed myelination could be assumed [126] –, further changes in $|G^*|$ were observed in the maturing brain. Upon cuprizone induction, a decrease in φ was noticed, which linearly correlated with progressive demyelination. Contrary to that, $|G^*|$ did not drop until 12 weeks, when peak demyelination was already reached. By relating $|G^*|$ to immunohistochemical markers, ECM alteration and lasting demyelination were both suggested as possible contributors to a loss in $|G^*|$.

Apart from demyelination and degeneration, inflammation itself should not be ignored as a potential confounding process on viscoelasticity. As suggested by Riek et al., in the murine brain, inflammation in the absence of demyelination induces a reversible reduction in $|G^*|$, which holds true for asymptomatic inflammation. Although patients undergoing relapse were excluded in the present study, the potential influence of subclinical inflammation present in MS has to be considered.

According to Schregel et al., one could hypothesize that $|G^*|$ reflects long-term microstructural alterations in MS. This consideration is in line with the data at hand, in which a reduction in $|G^*|$ was only independently explained by disease duration. However, as further stated by the authors, neither $|G^*|$ nor φ correlated with axonal injury, which was quantified by beta-amyloid precursor protein expression. Presuming causality between axonal damage and disability in MS, this complies with the present data, in which EDSS did not independently correlate with viscoelasticity alterations. Even more convincing, no significant difference between low and high EDSS subgroups was observed.

In trying to translate changes in $|G^*|$ and φ to structural correlates in MS, the following model was proposed by the research group around Sack et al.: $|G^*|$ reflects the connectivity between structural building blocks, also referred to as mechanical matrix, and is reduced from earliest stages of disease. φ describes the geometric alignment of these elements, which becomes only disturbed as the disease progresses [51, 54, 64].

However, this model is only partially compatible with data presented by Schregel et al. Moreover, neither approach provides further insight into this study's observed behavior of φ_{SGM}. Rheologically, a reduction in φ is defined as an increase in elasticity at a decrease in viscosity. Nevertheless, in the absence of studies or models consistent with the present findings, it is unfeasible to infer structural correlates or to propose a theoretical framework explaining this study's observations.

Despite a rise in literature on MS brain viscoelasticity and related animal models, research failed to identify a causal relationship between pathophysiological processes and viscoelasticity to date [51, 52, 127]. As pointed out above, numerous physiological and pathophysiological aspects are assumed to contribute to mechanical properties of tissue, resulting in a lack of specificity of $|G^*|$ and φ. This study's findings are therefore interpreted as a consequence of both physiological degeneration and MS pathology, which potentially give rise to combined as well as competing effects in viscoelasticity.

5.4 Strengths and Limitations

5.4.1 Image Acquisition

Both cohorts underwent identical MRI protocols, ensuring comparable results in later analysis due to consistent tissue contrast, e.g., in segmentation or atrophy estimation. Another strength of this study is the use of DENSE in MRE image acquisition at a low actuation frequency. Lower frequency waves become less attenuated as they pass through tissue, preserving high SNR in deep brain structures. However, this comes at cost of spatial resolution [107, 127], which was accounted for by evaluating mean of global regions or relatively large subregions.

In the literature on brain MRE, most authors use frequencies in the range of $25 - 62.5$ Hz [41, 51, 54, 98, 102] and facilitate echo-planar imaging (EPI) for information readout. However, gradient echoes as used in EPI are inherently affected by susceptibility artifacts [82, 85, 128]. By encoding phase information into M_z, in DENSE, information is robust to FID and related artifacts [84].

In the present MRE setup, a single actuation frequency was used, which is an obvious weakness for various reasons. As pointed out by Papazoglou et al. [129], reflections of shear waves at tissue interfaces are frequency-dependent. Moreover, a single-frequency setup is not robust to the formation of standing waves, resulting in low SNR in wave nodes [54, 130]. A multi-frequency setup could help to overcome these limitations, improve SNR and better address unknown effects. Evidently, this would come at cost of acquisition time, which, on the other hand, could be counterbalanced by slice number reduction.

However, a novel MRE acquisition protocol is a limitation in this study, since it impedes direct comparison to prior research.

5.4.2 Validity and Reliability of Viscoelasticity Data

A crucial step in the post-processing pipeline is inversion, which reconstructs a viscoelasticity map based on displacement data. The MDEV algorithm used in this study is well-established and has proven robust results in phantoms and *in vivo* [60, 76, 78, 86, 131]. However, typical for inversion algorithms, it presupposes brain tissue as continuous, homogenous and isotropic [77, 132]. Indentation testing and multi-directional MRE studies suggested isotropy in GM on a macroscopic scale [133]. Contrary to that, aligned fibres in WM, structurally anisotropic per se, were shown to exhibit a significant anisotropic behavior under compression [107, 132]. MRE studies addressing this problems exist [134] and in theory, multi-directional MRE experiments could account for this problem.

In addition, acquired viscoelasticity parameters are only valid within the brain's linear viscoelastic region (LVER). Strain stiffening and sensitivity to strain rate were pointed out to distort measurements [135] with variations in brain stiffness in the orders of magnitude, as recently shown by Herthum et al. [136].

Finally, due to its close proximity to the skull and CSF, the brain is encompassed by structures with opposing viscoelasticity, potentially leading to unpredictable behavior in wave propagation.

Physiological considerations stress the importance of tissue hydration status on brain viscoelasticity, which is also supported by a study on blood perfusion pressure dependency [106]. However, this was not considered in the present study. The experiment by Wuerfel et al. was accounting for this by performing measurements at the same time of day. Apart from practicality, whether this approach reliably addresses hydration state, is unclear. E.g., Murphy et al. stated robust test-retest results in MRE ranging between 1% and 2% ($N = 10$), which is why the significance of hydration status is questionable. For future research, one possible approach could be introducing a water intake protocol.

As for MS patients, there is evidence that cortisol therapy induces short-term brain volume changes by reducing intracellular water, which has to be considered in MRE during relapse therapy [137].

Taking everything into account, it remains surprising that in the data at hand and in previous research, measured viscoelasticities vary substantially among participants. Interestingly, this study found similar standard deviations between subregional and global ROIs, indicating that measured differences among subjects did not originate from poor SNR. Although there is strong evidence that data reflect true differences in microstructure, confounders cannot be ruled out, which is why further research is needed to verify validity of MRE experiments.

5.4.3 Participants

Compared to related studies, this work provided a considerable sample size, particularly in the MS cohort. However, a weakness is that cohorts did not match concerning age ($p < 0.001$) and size with an underrepresentation of healthy volunteers above the age of 30. One possible consequence is poor performance of statistical tests in terms of age, leading to lack of significance in HCs.

This study intended to explore the hypothesis that mechanical properties of the MS brain are affected by diffuse neurodegenerative processes. However, progressive phenotypes, the prototypes of diffuse parenchymal damage, were barely represented. Although it is known that diffuse neurodegeneration is present at early stages in both relapsing and progressive courses of disease [7, 8, 26, 57], proposed hypotheses could not be tested in progressive MS.

5.5 Conclusion

Whereas existing literature agrees on softening of brain tissue in MS, this study found no substantial alterations in brain viscoelasticity in patients. Similar to prior work, a large disparity in global viscoelasticity between subjects was observed. It can be therefore concluded that MRE lacks necessary sensitivity and specificity to assist MS diagnosis.

However, it cannot be inferred therefrom that MRE disqualifies as a candidate for longitudinal assessment of patients. In fact, this study confirmed the hypothesis that parenchymal degeneration is reflected by changes in viscoelasticity. Most notably, data suggested aging and brain atrophy to independently correlate with a decrease in φ_{SGM}, which was not reported in prior research.

The present data indicated consistent subregional characteristics in viscoelasticity across cohorts, which is why it can be inferred that analysis of localized processes is feasible in MRE. However, this study found no evidence that MRE can contribute to lesion characterization, albeit further research has to be done with the help of contrast-enhanced MRI modalities.

Nevertheless, as a modality capable of quantifying localized parenchymal changes, it can be assumed that with technical advances, MRE indeed has the potential to contribute to further understanding of disease.

For the most part, this study's observations are not in line with prior work. As a consequence, this work challenges existing models regarding pathophysiological correlates of viscoelasticity parameters. Due to a novel acquisition protocol, however, presented results are neither verifiable nor falsifiable to date. Thus, how this study's methodology performs in quantification of the actual mechanical properties of brain tissue, has to be investigated in future work.

5.6 Outlook

Since its first application in brain in 2008, various MRE protocols have been developed. However, even about allegedly fundamental questions, literature is ambiguous. Discrepancies in data of existing work highlight the necessity for standardized stiffness maps, which ideally incorporate data from different modalities and account for age and sex. Eventually, a ground truth in methodology has to be established, based on which acquisition protocols can undergo further refinement in order to explore different pathologies.

As a novel modality, technical improvements in spatial resolution and SNR can be expected, which increase both sensitivity and specificity. Multi-frequency studies can help eliminate frequency-dependent artifacts. Finally, novel inversion algorithms coupled with multi-directional actuation could account for WM anisotropy.

With the implementation of these aspects, MRE's role in MS assessment needs to be re-evaluated. In the future, longitudinal MRE examination could help to objectively quantify the temporal progression of diffuse neurodegeneration in patients. Thereby, MRE could contribute to understanding of disease and help to overcome the clinico-radiologic paradox. Ultimately, MRE may find its way into the neurologist's toolbox and assist to find the best long-term disease-modifying therapy for the individual patient.

References

[1] H. Kenneth Walker, W. Dallas Hall, and J. Willis Hurst, eds. *Clinical Methods: The History, Physical, and Laboratory Examinations*. 3rd. Boston: Butterworths, 1990. ISBN: 978-0-409-90077-4.

[2] Alan J. Thompson et al. “Multiple Sclerosis”. In: *Lancet (London, England)* 391.10130 (Apr. 2018), pp. 1622–1636. ISSN: 1474-547X. DOI: `10.1016/S0140-6736(18)30481-1`.

[3] Fred D. Lublin et al. “Defining the Clinical Course of Multiple Sclerosis: The 2013 Revisions”. In: *Neurology* 83.3 (July 2014), pp. 278–286. ISSN: 1526-632X. DOI: `10.1212/WNL.0000000000000560`.

[4] Bilge Piri Çinar and Serkan Özakbaş. “Prediction of Conversion from Clinically Isolated Syndrome to Multiple Sclerosis According to Baseline Characteristics: A Prospective Study”. In: *Noro Psikiyatri Arsivi* 55.1 (Mar. 2018), pp. 15–21. ISSN: 1300-0667. DOI: `10.29399/npa.12667`.

[5] Tomasz Grzegorski and Jacek Losy. “What Do We Currently Know about the Clinically Isolated Syndrome Suggestive of Multiple Sclerosis? An Update”. In: *Reviews in the Neurosciences* 31.3 (Apr. 2020), pp. 335–349. ISSN: 2191-0200, 0334-1763. DOI: `10.1515/revneuro-2019-0084`.

[6] Alan J Thompson et al. “Diagnosis of Multiple Sclerosis: 2017 Revisions of the McDonald Criteria”. In: *The Lancet Neurology* 17.2 (Feb. 2018), pp. 162–173. ISSN: 14744422. DOI: `10.1016/S1474-4422(17)30470-2`.

[7] Manuel A. Friese, Benjamin Schattling, and Lars Fugger. “Mechanisms of Neurodegeneration and Axonal Dysfunction in Multiple Sclerosis”. In: *Nature Reviews. Neurology* 10.4 (Apr. 2014), pp. 225–238. ISSN: 1759-4766. DOI: `10.1038/nrneurol.2014.37`.

[8] Hans Lassmann. “Pathology and Disease Mechanisms in Different Stages of Multiple Sclerosis”. In: *Journal of the Neurological Sciences* 333.1-2 (Oct. 2013), pp. 1–4. ISSN: 0022510X. DOI: `10.1016/j.jns.2013.05.010`.

[9] Carolyn Goldschmidt and Marisa P. McGinley. “Advances in the Treatment of Multiple Sclerosis”. In: *Neurologic Clinics* 39.1 (Feb. 2021), pp. 21–33. ISSN: 07338619. DOI: `10.1016/j.ncl.2020.09.002`.

[10] Gavin Giovannoni. “Disease-Modifying Treatments for Early and Advanced Multiple Sclerosis: A New Treatment Paradigm”. In: *Current Opinion in Neurology* 31.3 (June 2018), pp. 233–243. ISSN: 1473-6551. DOI: `10.1097/WCO.0000000000000561`.

[11] J. F. Kurtzke. “Rating Neurologic Impairment in Multiple Sclerosis: An Expanded Disability Status Scale (EDSS)”. In: *Neurology* 33.11 (Nov. 1983), pp. 1444–1452. ISSN: 0028-3878. DOI: `10.1212/wnl.33.11.1444`.

[12] Mike P. Wattjes et al. “Evidence-Based Guidelines: MAGNIMS Consensus Guidelines on the Use of MRI in Multiple Sclerosis–Establishing Disease Prognosis and Monitoring Patients”. In: *Nature Reviews. Neurology* 11.10 (Oct. 2015), pp. 597–606. ISSN: 1759-4766. DOI: `10.1038/nrneurol.2015.157`.

[13] Massimo Filippi et al. “MRI Criteria for the Diagnosis of Multiple Sclerosis: MAGNIMS Consensus Guidelines”. In: *The Lancet. Neurology* 15.3 (Mar. 2016), pp. 292–303. ISSN: 1474-4465. DOI: `10.1016/S1474-4422(15)00393-2`.

[14] Arnaud Charil et al. “MRI and the Diagnosis of Multiple Sclerosis: Expanding the Concept of "No Better Explanation"”. In: *The Lancet. Neurology* 5.10 (Oct. 2006), pp. 841–852. ISSN: 1474-4422. DOI: `10.1016/S1474-4422(06)70572-5`.

[15] D. T. Okuda et al. “Incidental MRI Anomalies Suggestive of Multiple Sclerosis: The Radiologically Isolated Syndrome”. In: *Neurology* 72.9 (Mar. 2009), pp. 800–805. ISSN: 1526-632X. DOI: `10.1212/01.wnl.0000335764.14513.1a`.

[16] Frederik Barkhof. “The Clinico-Radiological Paradox in Multiple Sclerosis Revisited”. In: *Current Opinion in Neurology* 15.3 (June 2002), pp. 239–245. ISSN: 1350-7540. DOI: `10.1097/00019052-200206000-00003`.

[17] Declan Chard and S. Anand Trip. “Resolving the Clinico-Radiological Paradox in Multiple Sclerosis”. In: *F1000Research* 6 (2017), p. 1828. ISSN: 2046-1402. DOI: `10.12688/f1000research.11932.1`.

[18] Kerstin Hackmack et al. “Can We Overcome the ’clinico-Radiological Paradox’ in Multiple Sclerosis?” In: *Journal of Neurology* 259.10 (Oct. 2012), pp. 2151–2160. ISSN: 1432-1459. DOI: `10.1007/s00415-012-6475-9`.

[19] Tomas Uher et al. “Cognitive Clinico-Radiological Paradox in Early Stages of Multiple Sclerosis”. In: *Annals of Clinical and Translational Neurology* 5.1 (Jan. 2018), pp. 81–91. ISSN: 23289503. DOI: `10.1002/acn3.512`.

[20] Thomas Zeis et al. “Normal-Appearing White Matter in Multiple Sclerosis Is in a Subtle Balance between Inflammation and Neuroprotection”. In: *Brain: A Journal of Neurology* 131.Pt 1 (Jan. 2008), pp. 288–303. ISSN: 1460-2156. DOI: `10.1093/brain/awm291`.

[21] D. L. Arnold et al. “Use of Proton Magnetic Resonance Spectroscopy for Monitoring Disease Progression in Multiple Sclerosis”. In: *Annals of Neurology* 36.1 (July 1994), pp. 76–82. ISSN: 0364-5134. DOI: `10.1002/ana.410360115`.

[22] Nicola De Stefano et al. “Magnetic Resonance Spectroscopy as a Measure of Brain Damage in Multiple Sclerosis”. In: *Journal of the Neurological Sciences* 233.1-2 (June 2005), pp. 203–208. ISSN: 0022-510X. DOI: `10.1016/j.jns.2005.03.018`.

[23] Nicola De Stefano et al. “Clinical Relevance of Brain Volume Measures in Multiple Sclerosis”. In: *CNS drugs* 28.2 (Feb. 2014), pp. 147–156. ISSN: 1179-1934. DOI: `10.1007/s40263-014-0140-z`.

[24] Raed Alroughani et al. “A Regional Consensus Recommendation on Brain Atrophy as an Outcome Measure in Multiple Sclerosis”. In: *BMC neurology* 16.1 (Nov. 2016), p. 240. ISSN: 1471-2377. DOI: `10.1186/s12883-016-0762-5`.

[25] Sarah Cappelle et al. “A Validation Study of Manual Atrophy Measures in Patients with Multiple Sclerosis”. In: *Neuroradiology* 62.8 (Aug. 2020), pp. 955–964. ISSN: 1432-1920. DOI: `10.1007/s00234-020-02401-3`.

[26] Asaff Harel et al. “Brain Microstructural Injury Occurs in Patients with RRMS despite 'No Evidence of Disease Activity'”. In: *Journal of Neurology, Neurosurgery, and Psychiatry* 89.9 (Sept. 2018), pp. 977–982. ISSN: 1468-330X. DOI: `10.1136/jnnp-2017-317606`.

[27] Sudhakar K Venkatesh and Richard L Ehman. *Magnetic Resonance Elastography.* New York, NY: Springer, 2014. ISBN: 978-1-4939-1575-0.

[28] Michael A. Green, Lynne E. Bilston, and Ralph Sinkus. “In Vivo Brain Viscoelastic Properties Measured by Magnetic Resonance Elastography”. In: *NMR in biomedicine* 21.7 (Aug. 2008), pp. 755–764. ISSN: 0952-3480. DOI: `10.1002/nbm.1254`.

[29] A Bertram. *Elasticity and Plasticity of Large Deformations: Including Gradient Materials.* 2021. ISBN: 978-3-030-72328-6.

[30] A. Bonfanti et al. “Fractional Viscoelastic Models for Power-Law Materials”. In: *Soft Matter* 16.26 (2020), pp. 6002–6020. ISSN: 1744-683X, 1744-6848. DOI: `10.1039/D0SM00354A`.

[31] J. a. W. van Dommelen et al. “Mechanical Properties of Brain Tissue by Indentation: Interregional Variation”. In: *Journal of the Mechanical Behavior of Biomedical Materials* 3.2 (Feb. 2010), pp. 158–166. ISSN: 1878-0180. DOI: `10.1016/j.jmbbm.2009.09.001`.

[32] Ingolf Sack. “Magnetresonanz-Elastographie”. In: 133 (2008), pp. 247–251. DOI: `10.1055/s-2008-1017505`.

[33] S. A. Kruse et al. “Tissue Characterization Using Magnetic Resonance Elastography: Preliminary Results”. In: *Physics in Medicine and Biology* 45.6 (June 2000), pp. 1579–1590. ISSN: 0031-9155. DOI: `10.1088/0031-9155/45/6/313`.

[34] R. A. Brooks. “A Quantitative Theory of the Hounsfield Unit and Its Application to Dual Energy Scanning”. In: *Journal of Computer Assisted Tomography* 1.4 (Oct. 1977), pp. 487–493. ISSN: 0363-8715. DOI: `10.1097/00004728-197710000-00016`.

[35] Matthew J. Paszek et al. “Tensional Homeostasis and the Malignant Phenotype”. In: *Cancer Cell* 8.3 (Sept. 2005), pp. 241–254. ISSN: 1535-6108. DOI: `10.1016/j.ccr.2005.08.010`.

[36] R. Muthupillai et al. “Magnetic Resonance Elastography by Direct Visualization of Propagating Acoustic Strain Waves”. In: *Science (New York, N.Y.)* 269.5232 (Sept. 1995), pp. 1854–1857. ISSN: 0036-8075. DOI: `10.1126/science.7569924`.

[37] A. Manduca et al. “Magnetic Resonance Elastography: Non-Invasive Mapping of Tissue Elasticity”. In: *Medical Image Analysis* 5.4 (Dec. 2001), pp. 237–254. ISSN: 13618415. DOI: `10.1016/S1361-8415(00)00039-6`.

[38] Kevin J. Glaser, Armando Manduca, and Richard L. Ehman. “Review of MR Elastography Applications and Recent Developments”. In: *Journal of Magnetic Resonance Imaging* 36.4 (Oct. 2012), pp. 757–774. ISSN: 10531807. DOI: `10.1002/jmri.23597`.

[39] Yogesh K. Mariappan, Kevin J. Glaser, and Richard L. Ehman. “Magnetic Resonance Elastography: A Review”. In: *Clinical Anatomy (New York, N.Y.)* 23.5 (July 2010), pp. 497–511. ISSN: 1098-2353. DOI: `10.1002/ca.21006`.

[40] Joo Yong Lee et al. “Stiffness of the Central Corpus Cavernosum on Shear-Wave Elastography Is Inversely Correlated with the Penile Rigidity Score in Patients with Erectile Dysfunction”. In: *The World Journal of Men’s Health* 39.1 (Jan. 2021), pp. 123–130. ISSN: 2287-4208. DOI: `10.5534/wjmh.190094`.

[41] Ingolf Sack et al. “The Impact of Aging and Gender on Brain Viscoelasticity”. In: *NeuroImage* 46.3 (July 2009), pp. 652–657. ISSN: 1095-9572. DOI: `10.1016/j.neuroimage.2009.02.040`.

[42] Ralph Sinkus et al. “MR Elastography of Breast Lesions: Understanding the Solid/Liquid Duality Can Improve the Specificity of Contrast-Enhanced MR Mammography”. In: *Magnetic Resonance in Medicine* 58.6 (Dec. 2007), pp. 1135–1144. ISSN: 07403194, 15222594. DOI: `10.1002/mrm.21404`.

[43] Siddharth Singh et al. “Diagnostic Performance of Magnetic Resonance Elastography in Staging Liver Fibrosis: A Systematic Review and Meta-Analysis of Individual Participant Data”. In: *Clinical Gastroenterology and Hepatology: The Official Clinical Practice Journal of the American Gastroenterological Association* 13.3 (Mar. 2015), 440–451.e6. ISSN: 1542-7714. DOI: `10.1016/j.cgh.2014.09.046`.

[44] Meng Yin et al. “Assessment of Hepatic Fibrosis with Magnetic Resonance Elastography”. In: *Clinical Gastroenterology and Hepatology: The Official Clinical Practice Journal of the American Gastroenterological Association* 5.10 (Oct. 2007), 1207–1213.e2. ISSN: 1542-7714. DOI: `10.1016/j.cgh.2007.06.012`.

[45] Ingolf Sack et al. “Non-Invasive Measurement of Brain Viscoelasticity Using Magnetic Resonance Elastography”. In: *NMR in biomedicine* 21.3 (Mar. 2008), pp. 265–271. ISSN: 0952-3480. DOI: `10.1002/nbm.1189`.

[46] Scott A. Kruse et al. “Magnetic Resonance Elastography of the Brain”. In: *NeuroImage* 39.1 (Jan. 2008), pp. 231–237. ISSN: 10538119. DOI: `10.1016/j.neuroimage.2007.08.030`.

[47] Lucy V. Hiscox et al. “Magnetic Resonance Elastography (MRE) of the Human Brain: Technique, Findings and Clinical Applications”. In: *Physics in Medicine and Biology* 61.24 (Dec. 2016), R401–R437. ISSN: 1361-6560. DOI: `10.1088/0031-9155/61/24/R401`.

[48] Gavin Low, Scott A. Kruse, and David J. Lomas. “General Review of Magnetic Resonance Elastography”. In: *World Journal of Radiology* 8.1 (Jan. 2016), pp. 59–72. ISSN: 1949-8470. DOI: `10.4329/wjr.v8.i1.59`.

[49] Kaspar-Josche Streitberger et al. “In Vivo Viscoelastic Properties of the Brain in Normal Pressure Hydrocephalus”. In: *NMR in biomedicine* 24.4 (May 2011), pp. 385–392. ISSN: 1099-1492. DOI: `10.1002/nbm.1602`.

[50] M. Reiss-Zimmermann et al. “High Resolution Imaging of Viscoelastic Properties of Intracranial Tumours by Multi-Frequency Magnetic Resonance Elastography”. In: *Clinical Neuroradiology* 25.4 (Dec. 2015), pp. 371–378. ISSN: 1869-1447. DOI: `10.1007/s00062-014-0311-9`.

[51] Kaspar-Josche Streitberger et al. “Brain Viscoelasticity Alteration in Chronic-Progressive Multiple Sclerosis”. In: *PloS One* 7.1 (2012), e29888. ISSN: 1932-6203. DOI: `10.1371/journal.pone.0029888`.

[52] Katharina Schregel et al. “Demyelination Reduces Brain Parenchymal Stiffness Quantified in Vivo by Magnetic Resonance Elastography”. In: *Proceedings of the National Academy of Sciences of the United States of America* 109.17 (Apr. 2012), pp. 6650–6655. ISSN: 1091-6490. DOI: `10.1073/pnas.1200151109`.

[53] Kerstin Riek et al. “Magnetic Resonance Elastography Reveals Altered Brain Viscoelasticity in Experimental Autoimmune Encephalomyelitis”. In: *NeuroImage. Clinical* 1.1 (2012), pp. 81–90. ISSN: 2213-1582. DOI: `10.1016/j.nicl.2012.09.003`.

[54] Jens Wuerfel et al. “MR-Elastography Reveals Degradation of Tissue Integrity in Multiple Sclerosis”. In: *NeuroImage* 49.3 (Feb. 2010), pp. 2520–2525. ISSN: 1095-9572. DOI: `10.1016/j.neuroimage.2009.06.018`.

[55] Matthew C. Murphy et al. “Decreased Brain Stiffness in Alzheimer’s Disease Determined by Magnetic Resonance Elastography”. In: *Journal of magnetic resonance imaging: JMRI* 34.3 (Sept. 2011), pp. 494–498. ISSN: 1522-2586. DOI: `10.1002/jmri.22707`.

[56] Mona ElSheikh et al. “MR Elastography Demonstrates Unique Regional Brain Stiffness Patterns in Dementias”. In: *AJR. American journal of roentgenology* 209.2 (Aug. 2017), pp. 403–408. ISSN: 1546-3141. DOI: `10.2214/AJR.16.17455`.

[57] Andreas Fehlner et al. “Higher-Resolution MR Elastography Reveals Early Mechanical Signatures of Neuroinflammation in Patients with Clinically Isolated Syndrome”. In: *Journal of magnetic resonance imaging: JMRI* 44.1 (July 2016), pp. 51–58. ISSN: 1522-2586. DOI: `10.1002/jmri.25129`.

[58] J. Weickenmeier et al. “Brain Stiffness Increases with Myelin Content”. In: *Acta Biomaterialia* 42 (Sept. 2016), pp. 265–272. ISSN: 1878-7568. DOI: `10.1016/j.actbio.2016.07.040`.

[59] Emad Moeendarbary et al. “The Soft Mechanical Signature of Glial Scars in the Central Nervous System”. In: *Nature Communications* 8.1 (Apr. 2017), p. 14787. ISSN: 2041-1723. DOI: `10.1038/ncomms14787`.

[60] Jing Guo et al. “Towards an Elastographic Atlas of Brain Anatomy”. In: *PloS One* 8.8 (2013), e71807. ISSN: 1932-6203. DOI: `10.1371/journal.pone.0071807`.

[61] Curtis L. Johnson et al. “Local Mechanical Properties of White Matter Structures in the Human Brain”. In: *NeuroImage* 79 (Oct. 2013), pp. 145–152. ISSN: 1095-9572. DOI: `10.1016/j.neuroimage.2013.04.089`.

[62] Jürgen Braun et al. “High-Resolution Mechanical Imaging of the Human Brain by Three-Dimensional Multifrequency Magnetic Resonance Elastography at 7T”. In: *NeuroImage* 90 (Apr. 2014), pp. 308–314. ISSN: 10538119. DOI: `10.1016/j.neuroimage.2013.12.032`.

[63] Grace McIlvain et al. “Mechanical Properties of the in Vivo Adolescent Human Brain”. In: *Developmental Cognitive Neuroscience* 34 (Nov. 2018), pp. 27–33. ISSN: 1878-9307. DOI: `10.1016/j.dcn.2018.06.001`.

[64] Ingolf Sack et al. “The Influence of Physiological Aging and Atrophy on Brain Viscoelastic Properties in Humans”. In: *PloS One* 6.9 (2011), e23451. ISSN: 1932-6203. DOI: `10.1371/journal.pone.0023451`.

[65] Arvin Arani et al. “Measuring the Effects of Aging and Sex on Regional Brain Stiffness with MR Elastography in Healthy Older Adults”. In: *NeuroImage* 111 (May 2015), pp. 59–64. ISSN: 1095-9572. DOI: `10.1016/j.neuroimage.2015.02.016`.

[66] Prateek Kalra et al. “Magnetic Resonance Elastography of Brain: Comparison between Anisotropic and Isotropic Stiffness and Its Correlation to Age”. In: *Magnetic Resonance in Medicine* 82.2 (Aug. 2019), pp. 671–679. ISSN: 1522-2594. DOI: `10.1002/mrm.27757`.

[67] Paul A. Janmey and Manfred Schliwa. “Rheology”. In: *Current biology: CB* 18.15 (Aug. 2008), R639–R641. ISSN: 0960-9822. DOI: `10.1016/j.cub.2008.05.001`.

[68] Hiong Yap Gan and Yee Cheong LAM. “Viscoelasticity”. In: *Encyclopedia of Microfluidics and Nanofluidics*. Ed. by Dongqing Li. Boston, MA: Springer US, 2008, pp. 2147–2155. ISBN: 978-0-387-48998-8. DOI: `10.1007/978-0-387-48998-8âĂĄ666`.

[69] Daniel T.N. Chen et al. “Rheology of Soft Materials”. In: *Annual Review of Condensed Matter Physics* 1.1 (Aug. 2010), pp. 301–322. ISSN: 1947-5454, 1947-5462. DOI: `10.1146/annurev-conmatphys-070909-104120`.

[70] Cornelis Storm et al. “Nonlinear Elasticity in Biological Gels”. In: *Nature* 435.7039 (May 2005), pp. 191–194. ISSN: 1476-4687. DOI: `10.1038/nature03521`.

[71] Jing Guo et al. “Fractal Network Dimension and Viscoelastic Powerlaw Behavior: II. An Experimental Study of Structure-Mimicking Phantoms by Magnetic Resonance Elastography”. In: *Physics in Medicine and Biology* 57.12 (June 2012), pp. 4041–4053. ISSN: 1361-6560. DOI: `10.1088/0031-9155/57/12/4041`.

[72] Ingolf Sack et al. “Structure-Sensitive Elastography: On the Viscoelastic Powerlaw Behavior of in Vivo Human Tissue in Health and Disease”. In: *Soft Matter* 9.24 (2013), p. 5672. ISSN: 1744-683X, 1744-6848. DOI: `10.1039/c3sm50552a`.

[73] John B. Weaver et al. “Brain Mechanical Property Measurement Using MRE with Intrinsic Activation”. In: *Physics in Medicine and Biology* 57.22 (Nov. 2012), pp. 7275–7287. ISSN: 1361-6560. DOI: `10.1088/0031-9155/57/22/7275`.

[74] Andreas Kirsch. *An Introduction to the Mathematical Theory of Inverse Problems.* Vol. 120. Applied Mathematical Sciences. New York, NY: Springer New York, 2011. DOI: `10.1007/978-1-4419-8474-6`.

[75] Siri F. Svensson et al. “Robustness of MR Elastography in the Healthy Brain: Repeatability, Reliability, and Effect of Different Reconstruction Methods”. In: *Journal of magnetic resonance imaging: JMRI* 53.5 (May 2021), pp. 1510–1521. ISSN: 1522-2586. DOI: `10.1002/jmri.27475`.

[76] Daniel Fovargue, David Nordsletten, and Ralph Sinkus. “Stiffness Reconstruction Methods for MR Elastography”. In: *NMR in biomedicine* 31.10 (Oct. 2018), e3935. ISSN: 1099-1492. DOI: `10.1002/nbm.3935`.

[77] Sebastian Papazoglou et al. “Multifrequency Inversion in Magnetic Resonance Elastography”. In: *Physics in Medicine and Biology* 57.8 (Apr. 2012), pp. 2329–2346. ISSN: 0031-9155, 1361-6560. DOI: `10.1088/0031-9155/57/8/2329`.

[78] Kaspar-Josche Streitberger et al. “Multifrequency Magnetic Resonance Elastography of the Brain Reveals Tissue Degeneration in Neuromyelitis Optica Spectrum Disorder”. In: *European Radiology* 27.5 (May 2017), pp. 2206–2215. ISSN: 1432-1084. DOI: `10.1007/s00330-016-4561-6`.

[79] J. P. Mugler and J. R. Brookeman. “Three-Dimensional Magnetization-Prepared Rapid Gradient-Echo Imaging (3D MP RAGE)”. In: *Magnetic Resonance in Medicine* 15.1 (July 1990), pp. 152–157. ISSN: 0740-3194. DOI: `10.1002/mrm.1910150117`.

[80] F. Nelson et al. “3D MPRAGE Improves Classification of Cortical Lesions in Multiple Sclerosis”. In: *Multiple Sclerosis (Houndmills, Basingstoke, England)* 14.9 (Nov. 2008), pp. 1214–1219. ISSN: 1352-4585. DOI: `10.1177/1352458508094644`.

[81] B. Tins et al. “Three-Dimensional Sampling Perfection with Application-Optimised Contrasts Using a Different Flip Angle Evolutions Sequence for Routine Imaging of the Spine: Preliminary Experience”. In: *The British Journal of Radiology* 85.1016 (Aug. 2012), e480–489. ISSN: 1748-880X. DOI: `10.1259/bjr/25760339`.

[82] A. H. Aletras et al. “DENSE: Displacement Encoding with Stimulated Echoes in Cardiac Functional MRI”. In: *Journal of Magnetic Resonance (San Diego, Calif.: 1997)* 137.1 (Mar. 1999), pp. 247–252. ISSN: 1090-7807. DOI: `10.1006/jmre.1998.1676`.

[83] Daniel Kim et al. “Myocardial Tissue Tracking with Two-Dimensional Cine Displacement-Encoded MR Imaging: Development and Initial Evaluation”. In: *Radiology* 230.3 (Mar. 2004), pp. 862–871. ISSN: 0033-8419. DOI: `10.1148/radiol.2303021213`.

[84] Benjamin Robert et al. “Application of DENSE-MR-Elastography to the Human Heart”. In: *Magnetic Resonance in Medicine* 62.5 (Nov. 2009), pp. 1155–1163. ISSN: 1522-2594. DOI: `10.1002/mrm.22124`.

[85] Johannes Strasser et al. “Magnetic Resonance Elastography of the Human Brain Using a Multiphase DENSE Acquisition”. In: *Magnetic Resonance in Medicine* 81.6 (June 2019), pp. 3578–3587. ISSN: 1522-2594. DOI: `10.1002/mrm.27672`.

[86] Sebastian Hirsch et al. “MR Elastography of the Liver and the Spleen Using a Piezoelectric Driver, Single-Shot Wave-Field Acquisition, and Multifrequency Dual Parameter Reconstruction”. In: *Magnetic Resonance in Medicine* 71.1 (Jan. 2014), pp. 267–277. ISSN: 1522-2594. DOI: `10.1002/mrm.24674`.

[87] Florian Dittmann et al. “In Vivo Wideband Multifrequency MR Elastography of the Human Brain and Liver”. In: *Magnetic Resonance in Medicine* 76.4 (Oct. 2016), pp. 1116–1126. ISSN: 1522-2594. DOI: `10.1002/mrm.26006`.

[88] Bruce Fischl et al. “Sequence-Independent Segmentation of Magnetic Resonance Images”. In: *NeuroImage* 23 Suppl 1 (2004), S69–84. ISSN: 1053-8119. DOI: `10.1016/j.neuroimage.2004.07.016`.

[89] Paul Schmidt and Lucie Wink. *LST: A Lesion Segmentation Tool for SPM Manual/Documentation for Version 3.0.0.* 2019.

[90] TotalBoox and TBX. *Statistical Parametric Mapping: The Analysis of Functional Brain Images.* Elsevier Science, 2011. ISBN: 978-0-08-046650-7.

[91] Chunjie Guo et al. “Repeatability and Reproducibility of FreeSurfer, FSL-SIENAX and SPM Brain Volumetric Measurements and the Effect of Lesion Filling in Multiple Sclerosis”. In: *European Radiology* 29.3 (Mar. 2019), pp. 1355–1364. ISSN: 0938-7994, 1432-1084. DOI: `10.1007/s00330-018-5710-x`.

[92] D Pareto et al. “Lesion Filling Effect in Regional Brain Volume Estimations: A Study in Multiple Sclerosis Patients with Low Lesion Load”. In: *Neuroradiology* 58.5 (May 2016), pp. 467–474. ISSN: 0028-3940, 1432-1920. DOI: `10.1007/s00234-016-1654-5`.

[93] R.W. Cox et al. “A (Sort of) New Image Data Format Standard: NiFTI-1”. In: vol. 22. 10th Annual Meeting of the Organization for Human Brain Mapping. Jan. 2004.

[94] Stephen M. Smith et al. “Advances in Functional and Structural MR Image Analysis and Implementation as FSL”. In: *NeuroImage* 23 Suppl 1 (2004), S208–219. ISSN: 1053-8119. DOI: `10.1016/j.neuroimage.2004.07.051`.

[95] Mark Jenkinson et al. “FSL”. In: *NeuroImage* 62.2 (Aug. 2012), pp. 782–790. ISSN: 1095-9572. DOI: `10.1016/j.neuroimage.2011.09.015`.

[96] Mark W. Woolrich et al. “Bayesian Analysis of Neuroimaging Data in FSL”. In: *NeuroImage* 45.1 Suppl (Mar. 2009), S173–186. ISSN: 1095-9572. DOI: `10.1016/j.neuroimage.2008.10.055`.

[97] M.M. Weeda et al. “Comparing Lesion Segmentation Methods in Multiple Sclerosis: Input from One Manually Delineated Subject Is Sufficient for Accurate Lesion Segmentation”. In: *NeuroImage: Clinical* 24 (2019), p. 102074. ISSN: 22131582. DOI: `10.1016/j.nicl.2019.102074`.

[98] Matthew C. Murphy et al. “Measuring the Characteristic Topography of Brain Stiffness with Magnetic Resonance Elastography”. In: *PloS One* 8.12 (2013), e81668. ISSN: 1932-6203. DOI: `10.1371/journal.pone.0081668`.

[99] Stephen M. Smith. “Fast Robust Automated Brain Extraction”. In: *Human Brain Mapping* 17.3 (Nov. 2002), pp. 143–155. ISSN: 1065-9471. DOI: `10.1002/hbm.10062`.

[100] Robert McGill, John W. Tukey, and Wayne A. Larsen. “Variations of Box Plots”. In: *The American Statistician* 32.1 (Feb. 1978), p. 12. ISSN: 00031305. DOI: `10.2307/2683468`.

[101] Lucy V. Hiscox et al. “Standard-Space Atlas of the Viscoelastic Properties of the Human Brain”. In: *Human Brain Mapping* 41.18 (Dec. 2020), pp. 5282–5300. ISSN: 1097-0193. DOI: `10.1002/hbm.25192`.

[102] Curtis L. Johnson et al. “Viscoelasticity of Subcortical Gray Matter Structures”. In: *Human Brain Mapping* 37.12 (Dec. 2016), pp. 4221–4233. ISSN: 1097-0193. DOI: `10.1002/hbm.23314`.

[103] K. J. Parker, T. Szabo, and S. Holm. “Towards a Consensus on Rheological Models for Elastography in Soft Tissues”. In: *Physics in Medicine and Biology* 64.21 (Oct. 2019), p. 215012. ISSN: 1361-6560. DOI: `10.1088/1361-6560/ab453d`.

[104] David E. Koser et al. “CNS Cell Distribution and Axon Orientation Determine Local Spinal Cord Mechanical Properties”. In: *Biophysical Journal* 108.9 (May 2015), pp. 2137–2147. ISSN: 00063495. DOI: `10.1016/j.bpj.2015.03.039`.

[105] T. Kaster, I. Sack, and A. Samani. “Measurement of the Hyperelastic Properties of Ex Vivo Brain Tissue Slices”. In: *Journal of Biomechanics* 44.6 (Apr. 2011), pp. 1158–1163. ISSN: 00219290. DOI: `10.1016/j.jbiomech.2011.01.019`.

[106] Stefan Hetzer et al. “Perfusion Alters Stiffness of Deep Gray Matter”. In: *Journal of Cerebral Blood Flow and Metabolism: Official Journal of the International Society of Cerebral Blood Flow and Metabolism* 38.1 (Jan. 2018), pp. 116–125. ISSN: 1559-7016. DOI: `10.1177/0271678X17691530`.

[107] Y. Feng et al. “Viscoelastic Properties of the Ferret Brain Measured in Vivo at Multiple Frequencies by Magnetic Resonance Elastography”. In: *Journal of Biomechanics* 46.5 (Mar. 2013), pp. 863–870. ISSN: 1873-2380. DOI: `10.1016/j.jbiomech.2012.12.024`.

[108] Silvia Budday et al. “Mechanical Properties of Gray and White Matter Brain Tissue by Indentation”. In: *Journal of the Mechanical Behavior of Biomedical Materials* 46 (June 2015), pp. 318–330. ISSN: 1878-0180. DOI: `10.1016/j.jmbbm.2015.02.024`.

[109] Paul J. McCracken et al. “Mechanical Transient-Based Magnetic Resonance Elastography”. In: *Magnetic Resonance in Medicine* 53.3 (Mar. 2005), pp. 628–639. ISSN: 0740-3194. DOI: `10.1002/mrm.20388`.

[110] Michael T. Prange and Susan S. Margulies. “Regional, Directional, and Age-Dependent Properties of the Brain Undergoing Large Deformation”. In: *Journal of Biomechanical Engineering* 124.2 (Apr. 2002), pp. 244–252. ISSN: 0148-0731. DOI: `10.1115/1.1449907`.

[111] Benjamin S. Elkin, Ashok I. Ilankovan, and Barclay Morrison. “A Detailed Viscoelastic Characterization of the P17 and Adult Rat Brain”. In: *Journal of Neurotrauma* 28.11 (Nov. 2011), pp. 2235–2244. ISSN: 1557-9042. DOI: `10.1089/neu.2010.1604`.

[112] Alireza Minagar et al. “The Thalamus and Multiple Sclerosis: Modern Views on Pathologic, Imaging, and Clinical Aspects”. In: *Neurology* 80.2 (Jan. 2013), pp. 210–219. ISSN: 1526-632X. DOI: `10.1212/WNL.0b013e31827b910b`.

[113] Alberto Cifelli et al. “Thalamic Neurodegeneration in Multiple Sclerosis”. In: *Annals of Neurology* 52.5 (Nov. 2002), pp. 650–653. ISSN: 0364-5134. DOI: `10.1002/ana.10326`.

[114] Marco Vercellino et al. “Demyelination, Inflammation, and Neurodegeneration in Multiple Sclerosis Deep Gray Matter”. In: *Journal of Neuropathology and Experimental Neurology* 68.5 (May 2009), pp. 489–502. ISSN: 0022-3069. DOI: `10.1097/NEN.0b013e3181a19a5a`.

[115] Dániel Sandi et al. “Neurodegeneration in Multiple Sclerosis: Symptoms of Silent Progression, Biomarkers and Neuroprotective Therapy-Kynurenines Are Important Players”. In: *Molecules (Basel, Switzerland)* 26.11 (June 2021), p. 3423. ISSN: 1420-3049. DOI: `10.3390/molecules26113423`.

[116] R. A. Rudick et al. “Use of the Brain Parenchymal Fraction to Measure Whole Brain Atrophy in Relapsing-Remitting MS. Multiple Sclerosis Collaborative Research Group”. In: *Neurology* 53.8 (Nov. 1999), pp. 1698–1704. ISSN: 0028-3878. DOI: `10.1212/wnl.53.8.1698`.

[117] Loredana Storelli et al. "Measurement of Whole-Brain and Gray Matter Atrophy in Multiple Sclerosis: Assessment with MR Imaging". In: *Radiology* 288.2 (Aug. 2018), pp. 554–564. ISSN: 0033-8419, 1527-1315. DOI: `10.1148/radiol.2018172468`.

[118] R. Zivadinov et al. "Mechanisms of Action of Disease-Modifying Agents and Brain Volume Changes in Multiple Sclerosis". In: *Neurology* 71.2 (July 2008), pp. 136–144. ISSN: 1526-632X. DOI: `10.1212/01.wnl.0000316810.01120.05`.

[119] Volker Siffrin et al. "Multiple Sclerosis - Candidate Mechanisms Underlying CNS Atrophy". In: *Trends in Neurosciences* 33.4 (Apr. 2010), pp. 202–210. ISSN: 1878-108X. DOI: `10.1016/j.tins.2010.01.002`.

[120] Josa M. Frischer et al. "Clinical and Pathological Insights into the Dynamic Nature of the White Matter Multiple Sclerosis Plaque: Dynamic Nature of MS Plaque". In: *Annals of Neurology* 78.5 (Nov. 2015), pp. 710–721. ISSN: 03645134. DOI: `10.1002/ana.24497`.

[121] Bogdan F. Gh Popescu, Istvan Pirko, and Claudia F. Lucchinetti. "Pathology of Multiple Sclerosis: Where Do We Stand?" In: *Continuum (Minneapolis, Minn.)* 19.4 Multiple Sclerosis (Aug. 2013), pp. 901–921. ISSN: 1538-6899. DOI: `10.1212/01.CON.0000433291.23091.65`.

[122] Massimo Filippi et al. "Assessment of Lesions on Magnetic Resonance Imaging in Multiple Sclerosis: Practical Guidelines". In: *Brain: A Journal of Neurology* 142.7 (July 2019), pp. 1858–1875. ISSN: 1460-2156. DOI: `10.1093/brain/awz144`.

[123] Mateusz M. Urbanski, Matthew B. Brendel, and Carmen V. Melendez-Vasquez. "Acute and Chronic Demyelinated CNS Lesions Exhibit Opposite Elastic Properties". In: *Scientific Reports* 9.1 (Dec. 2019), p. 999. ISSN: 2045-2322. DOI: `10.1038/s41598-018-37745-7`.

[124] Martina Absinta et al. "Association of Chronic Active Multiple Sclerosis Lesions With Disability In Vivo". In: *JAMA neurology* 76.12 (Dec. 2019), pp. 1474–1483. ISSN: 2168-6157. DOI: `10.1001/jamaneurol.2019.2399`.

[125] Florian Baptist Freimann et al. "MR Elastography in a Murine Stroke Model Reveals Correlation of Macroscopic Viscoelastic Properties of the Brain with Neuronal Density". In: *NMR in biomedicine* 26.11 (Nov. 2013), pp. 1534–1539. ISSN: 1099-1492. DOI: `10.1002/nbm.2987`.

[126] J. M. Matthieu, S. Widmer, and N. Herschkowitz. "Biochemical Changes in Mouse Brain Composition during Myelination". In: *Brain Research* 55.2 (June 1973), pp. 391–402. ISSN: 0006-8993. DOI: `10.1016/0006-8993(73)90304-1`.

[127] Matthew C. Murphy, John Huston, and Richard L. Ehman. "MR Elastography of the Brain and Its Application in Neurological Diseases". In: *NeuroImage* 187 (Feb. 2019), pp. 176–183. ISSN: 1095-9572. DOI: `10.1016/j.neuroimage.2017.10.008`.

[128] Robert W. Brown et al. *Magnetic Resonance Imaging: Physical Principles and Sequence Design*. Second edition. Hoboken, New Jersey: John Wiley & Sons, Inc, 2014. ISBN: 978-0-471-72085-0.

[129] S Papazoglou et al. "Horizontal Shear Wave Scattering from a Nonwelded Interface Observed by Magnetic Resonance Elastography". In: *Physics in Medicine and Biology* 52.3 (Feb. 2007), pp. 675–684. ISSN: 0031-9155, 1361-6560. DOI: `10.1088/0031-9155/52/3/010`.

[130] Curtis L. Johnson and Eva H. Telzer. "Magnetic Resonance Elastography for Examining Developmental Changes in the Mechanical Properties of the Brain". In: *Developmental Cognitive Neuroscience* 33 (Oct. 2018), pp. 176–181. ISSN: 1878-9307. DOI: `10.1016/j.dcn.2017.08.010`.

[131] Sebastian Hirsch, Jürgen Braun, and Ingolf Sack. *Magnetic Resonance Elastography: Physical Background and Medical Applications*. Weinheim: Wiley-VCH Verlag, 2016. ISBN: 978-3-527-34008-8.

[132] Aaron T. Anderson et al. "Observation of Direction-Dependent Mechanical Properties in the Human Brain with Multi-Excitation MR Elastography". In: *Journal of the Mechanical Behavior of Biomedical Materials* 59 (June 2016), pp. 538–546. ISSN: 1878-0180. DOI: `10.1016/j.jmbbm.2016.03.005`.

[133] Michael Prange and David F. Meaney. "Defining Brain Mechanical Properties: Effects of Region, Direction, and Species". In: *44th Stapp Car Crash Conference (2000)*. Nov. 2000, 2000-01–SC15. DOI: `10.4271/2000-01-SC15`.

[134] Anthony Romano et al. "In Vivo Waveguide Elastography of White Matter Tracts in the Human Brain". In: *Magnetic Resonance in Medicine* 68.5 (Nov. 2012), pp. 1410–1422. ISSN: 1522-2594. DOI: `10.1002/mrm.24141`.

[135] Ilya Levental, Penelope C. Georges, and Paul A. Janmey. "Soft Biological Materials and Their Impact on Cell Function". In: *Soft Matter* 3.3 (2007), pp. 299–306. ISSN: 1744-683X, 1744-6848. DOI: `10.1039/B610522J`.

[136] Helge Herthum et al. "Superviscous Properties of the in Vivo Brain at Large Scales". In: *Acta Biomaterialia* 121 (Feb. 2021), pp. 393–404. ISSN: 1878-7568. DOI: `10.1016/j.actbio.2020.12.027`.

[137] Robert Zivadinov. "Steroids and Brain Atrophy in Multiple Sclerosis". In: *Journal of the Neurological Sciences* 233.1-2 (June 2005), pp. 73–81. ISSN: 0022510X. DOI: `10.1016/j.jns.2005.03.006`.